TAMPEREEN TEKNILLINEN YLIOPISTO
TAMPERE UNIVERSITY OF TECHNOLOGY

UMAIR AHMED

DESIGN AND EXPERIMENTAL VERIFICATION OF MAGNETO-MECHANICAL ENERGY HARVESTING CONCEPT BASED ON CONSTRUCTION STEEL

Master of Science thesis

Examiner: Assist. Prof. Paavo Rasilo
Examiner and topic approved by the Council of the Faculty of Computing and Electrical Engineering on 8th June 2016

ABSTRACT

UMAIR AHMED: Design and experimental verification of magneto-mechanical energy harvesting concept based on construction steel.
Tampere University of technology
Master of Science Thesis, 73 pages
December 2016
Master's Degree Programme in Electrical Engineering.
Major: Smart Grids
Examiner: Assist. Prof. Paavo Rasilo
Keywords: buckling load, energy harvesting, flux density, magnetostriction, magnetic field, mechanical stress, magnetic saturation, permeability, Villari effect.

The development of self-powered system for powering small scale power electronic devices such as wireless networks and nodes, radio frequency based tags or readers and wireless sensors for applications like structural condition monitoring (SCM) and wireless data recording are getting very popular. The integration of vibration based energy harvesters with the above mentioned devices is a promising approach towards self-powered systems. The techniques of vibration based energy harvesting involve utilization of either piezo-electric or magnetostrictive materials. However, the active materials mostly employed in energy harvesters are either too expensive or are not commonly available. The objective of the study is to utilize construction material more specifically structural steel as an active material because of its abundant availability and practical applications in bridges buildings and rail tracks etc.

The literature study regarding various energy harvesting techniques and their applications are presented first to emphasize the importance of vibration based energy harvesting. The prototype design of the proposed energy harvester including the design of mechanical grips and magnetic circuit are discussed in detail. Three different test samples are utilized in which two samples are constructed in the form of a stack using 1 mm and 1.5 mm thick steel sheets and the third sample is a solid steel bar with the dimensions of 20 mm x 20 mm. The free length and cross-sectional area of each sample are 100 mm and 400 mm^2 respectively. The measurement method developed for single steel tester is utilized and a new method for obtaining magnetization curves is proposed in the study. In order to determine the effect of stress on magnetization curves, the test sample is first stressed statically using AC magnetization to obtain the stress dependent magnetization curves. It is observed that the permeability of the test material changes under tensile and compressive stress showing the stress dependent magnetic characteristic of the material. To experimentally verify the validity of measurement method and the proposed method, the test sample is stressed dynamically using DC magnetization inducing voltage in the pickup coil. The induced voltage is because of the inverse magnetostriction also known as Villari effect.

The results from the solid steel sample and the sample made up of steel sheets are compared during cyclic loading. The steel sheet sample does not go into saturation because of the changing magnetic circuit length as well as the air gap caused by the buckling of individual sheets. Whereas, the induced voltage from the pickup coil starts dropping in case of solid sample which shows that the material is reaching saturation. To validate the magnetization curves obtained from the proposed method, the magnetizing current (I) for

maximum ΔB (change in flux density) is calculated which is compared with the I at peak amplitude of the induced voltage curve. The results from the calculations do not take into the account the eddy current losses or hysteresis and therefore the measured results deviate slightly from the calculated results. The maximum power is measured at the point of maximum ΔB value by varying the load resistance for two different cases of cyclic loading. The average output power is measured 13.3 μW for cyclic loading from zero to -20 MPa and 8.76 μW for cyclic loading from 2.5 to 25 MPa at 11 Hz of mechanical vibration using 2.62 Ω load resistance.

PREFACE

This thesis has been written based on my work as a research assistant at the department of Electrical Engineering in Tampere University of Technology. It was an honor to work with Assistant Professor Mr. Paavo Rasilo on the project of energy harvesting.

I would like to thank Paavo for his suggestions, support and guidance to carry out the research work during my thesis. The way he guided me throughout the thesis made it very easy for me to work in a field which was not quite familiar to me before. I would also like to thank Mr. Jarmo Poulata for his help and patience to carry out the experimental work. I would like to pay my regards to Professor Mr. Pekka Ruuskanen for his help and advice in understanding the subject matters. The research work was funded by the strategic funds provided by TUT, so I would like to pay my gratitude to TUT for the funds. I really appreciate the technical help provided by Mr. Lasse Soderlund and his co-workers during hardware development.

Finally, I would like to thank my family members, my sister, my brother specially Mr. Attique Iqbal for their support and prayers during my Master's studies. I would dedicate this thesis to my beloved mother as she prayed for this moment to come. Last but not the least I would like to thank God for providing me the opportunity to come this far and for His countless blessings.

Tampere, 22.11.2016.

Umair Ahmed.

CONTENTS

LIST OF SYMBOLS AND ABBREVIATIONS

AC	alternating current
ADC	analog to digital converter
CAD	computer aided design
DC	direct current
GMM	giant magnetostrictive material
MSMAs	magnetic shape memory alloys
MLC	magneto-electric laminate composite
MEH	magnetostrictive energy harvesting
PCB	printed circuit board
PVDF	ploy vinyldene fluoride
RMA	root mean square
RF	radio frequency
RFID	radio frequency identification
SMA	shape memory alloy
SCM	structural condition monitoring

A	area
B	magnetic flux density
ΔB	change in flux density
Co	cobalt
F	force
Fe	iron
F_g	gauge factor
Ga	gallium
H	magnetic field intensity
I	moment of inertia
J	current density
K	coefficient of end boundary condition
k	mechanical coupling coefficient
Le	effective length
$\Delta \ell$	change in length
N	number of turns
Na	sodium
Ni	nickel
Pb	lead
PZT	lead zirconate titante
R	radius of gyration
Tc	Curie temperature
V	voltage
λ	slenderness ratio
μ	permeability of the material
μ_0	permeability of free space
μ_r	relative permeability
σ	stress

1. INTRODUCTION

Due to advancement in technology and fabrication of small scale power electronic devices, power requirement has been reduced to milliwatts and microwatts for devices like RF based sensors, wireless network systems, wearable electronic devices and implanted devices etc. [1]. Self-powered systems are nowadays getting more popular because of their usability in situations where it is not possible to have a power source readily available or the cost of replacement for the battery or its maintenance is quite high [2]. Most importantly for remote locations, battery replacement is quite laborious and cumbersome.

Need for self-powered devices gives rise to techniques where energy can be harvested from ambient sources and transferred to small scale power electronic devices. Energy harvesting techniques allow wireless or portable systems to be autonomous and battery free [3]. From the past few years, different kinds of vibration based energy harvesting techniques have been developed each having their own advantages and limitations. Various techniques developed to harvest energy can be classified based on their feasibility, maximum output power and energy density, thus, the utilization of these methods strongly depends upon the nature and type of the application [4].

1.1 The aim and motivation

Vibration based energy harvesting techniques developed so far utilizes either piezo-electric materials (polyvinylidene fluoride and lead zirconate titanate etc.) or giant magnetostrictive materials (Terfenol-D, Galfenol and thin film Metglas alloy). Such materials are either too expensive or are not commonly available. Also, to harvest energy using above mentioned materials first requires their integration to the structure from which the vibrational energy is to be extracted. The aim of the thesis was to design an energy harvesting device utilizing commonly available construction materials having ferromagnetic properties. Therefore, structural steel was selected as a test subject because the magnetic properties of structural steel such as permeability shows stress dependence.

The first step was to determine how permeability of the material changes when the material is subjected to different values of tensile and compressive stress. The measurement method developed in [5] was utilized to first obtain the magnetizing current as a function of flux density and stress ($I(\sigma, B)$) which was then utilized by the new proposed method to obtain the magnetization curves (B-H curves). The next step was to design a prototype of an energy harvesting device in order to validate the calculations from the proposed method and to experimentally verify the measured results. Finally, the feasibility of the structural steel in energy harvesting applications was to be determined by experimentally

measuring the average output power the device can deliver under specific cyclic loading conditions.

1.2 The scope

In the area of structural condition monitoring, low power wireless sensors and networks play very important role in remotely monitoring the status of the structural condition. Furthermore, non-destructive structural condition monitoring demands continuous monitoring of the sensor's data. Most wireless sensors require battery for their operation which has limited life-span, also, the battery needs replacement which it gets discharged. Therefore, application like condition monitoring where the reliability and continuity of power supply is crucial, the role of energy harvesting devices comes into play. The energy harvested from ambient vibrational sources enable wireless sensors to be autonomous and self-powered. The power requirement of wireless sensors has been reduced up to 100s and 10s of microwatts making energy harvesting devices even more favorable to be employed as power source. For example, an ultralow power microprocessor PIC16F1508 require 30 µW to 200 µW to process the data coming from wireless sensor [3]. Thus, vibration based energy harvester proposed in the thesis will allow maintenance and battery free applications for devices which require low power for their operation.

The background studies regarding energy harvesting devices, their working principle and the amount of energy that can be harvested are presented in Chapter 2. The applications of vibration based energy harvesting devices are presented in Chapter 3. The mechanical design and working principle of the proposed energy harvesting device are explained in Chapter 4. The measurement method and experimental methods developed to determine the magnetization curves for the test sample are presented in Chapter 5. The *B*-*H* curves obtained based on the proposed method under static stress and the experimental results of induced voltage from the pickup coil and the corresponding average power obtained by cyclic loading of the test sample are presented in Chapter 6. The discussion regarding results obtained by proposed measurement method and experimentation, possible sources of errors, limitation of the device design and deviation from expected results is given in Chapter 7. Finally, the conclusion and possible future work are presented in Chapter 8.

2. REVIEW OF ENERGY HARVESTING DEVICES

This chapter presents the state of the art review of energy harvesting devices that have been developed so far. Various techniques developed utilizing ambient sources of energy have been discussed briefly. Examples are given for each technique elaborating the working principle of the energy harvester and the results have been discussed to compare the energy density for different devices. The main focus is related to vibration based energy harvesting utilizing either magnetostrictive and piezo-electric materials. Each technique has its own advantages and limitations, thus their utilization strongly depends upon the type of the application and its feasibility. Potential ways of energy scavenging are given in the following section which include solar power, electrostatic, micro turbine generators, magnetostrictive, piezo electric, micro fuel cells and electromagnetic energy [4].

2.1 Ambient sources of energy

Ambient energy sources being utilized to harvest energy are explained briefly. The sources of energy (thermal energy, light energy, mechanical energy, electromagnetic energy and RF energy) are classified based on their nature and characteristics [3], [6].

2.1.1 Vibrational energy

Ambient vibrations from skyscrapers, rail tracks, bridges, body of cars, mechanical stress and strain etc. are possible sources of vibrational energy. Vibrational energy is converted into electrical energy by variety of ways utilizing different smart materials. The frequency and amplitude of vibration are important parameters for vibration based energy harvesting [7].

2.1.2 Radio frequency energy

The potential sources of RF (radio frequency) energy are ambient or controlled RF radiations. The RF radiations are captured from electromagnetic waves that can be directly converted to electricity using electronic circuitry which is further explained in [8]. The captured power can be utilized to power wireless sensor networks operating at very low power.

2.1.3 Thermal energy

Possible sources of thermal energy involve heat produced by burning of coal, natural gas, biofuels or by frictional force etc. Energy harvesting using thermoelectric principle in-

volves utilization of smart materials (piezo-electric, magnetostrictive, shape memory alloys etc.) [9]. The temperature gradient is converted directly into electricity based on thermoelectric effect.

2.1.4 Light energy

Solar energy or light from indoor incandescent lamps etc. are possible sources of light energy. Photovoltaic cells convert natural or artificial light energy to electricity. The amount of electricity produced depends on the intensity of light and material used for the conversion of light energy. For example, silicon or gallium arsenide materials can absorb moderate amount of energy but their conversion efficiency is more as compared to thin film solar cells [10].

The utilization of above mentioned energy resources depends upon their feasibility and intended applications. To generalize the idea, few examples are given in Figure 2.1 [3] briefly describing the processes involved from utilization of potential ambient sources to energy harvesting and storage.

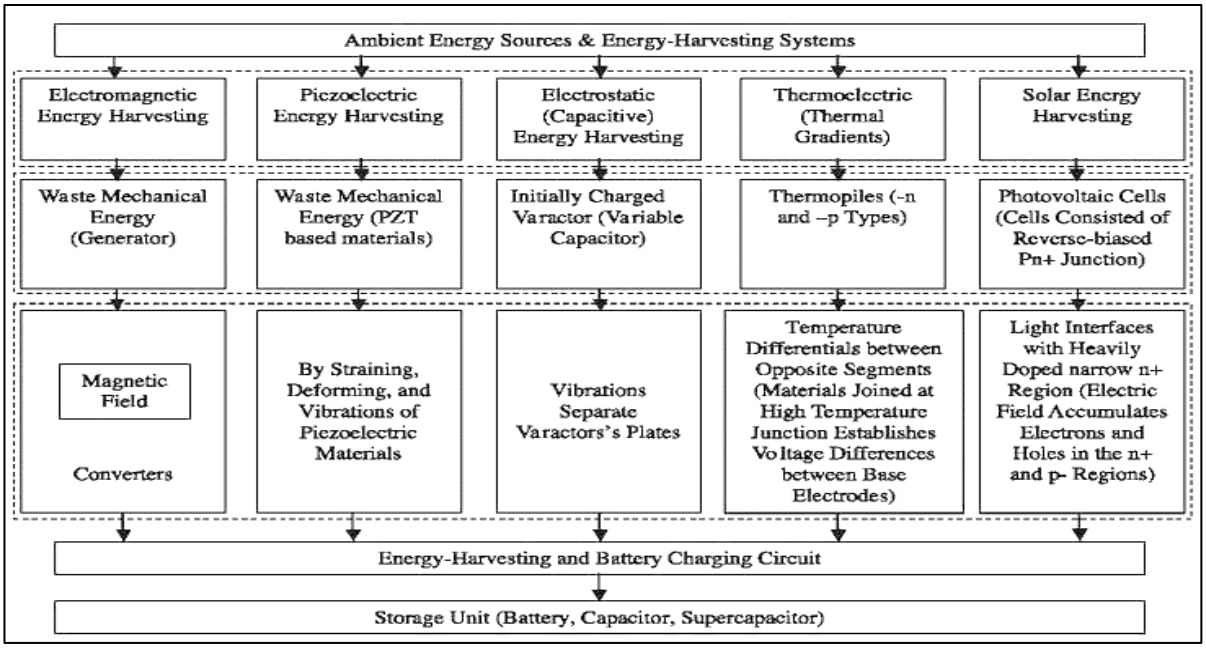

Figure 2.1: *Methods and processes involved in ambient energy harvesting system [3].*

2.2 An overview of magnetostrictive and piezo-electric materials.

Energy harvesting through ambient vibrations involves utilization of magnetic shape memory alloy (MSMA), magnetostrictive or piezo-electric materials also known as smart materials. Piezo-electric materials were first discovered by two brothers Pierre Curie and Jacques Curie back in 1880 whereas the discovery of magnetostrictive materials occurred

in 1960's when two rare earth elements terbium and dysprosium were manufactured [11], [12]. The physical phenomena and properties of magnetostrictive and piezo-electric materials are discussed in the following section.

2.2.1 Magnetostrictive materials

Joule's effect discovered by James Prescott Joule in 1842 was the most important discovery in the field of magnetostrictive materials. Magnetostrictive properties exist in ferromagnetic materials which can broadly be defined as change in shape or size of the material when it is subjected to an external magnetic field [13]. The phenomenon is known as magnetostriction. The concept of magnetostriction is explained in Figure 2.2 where applied magnetic field causes change in the length of the material [14].

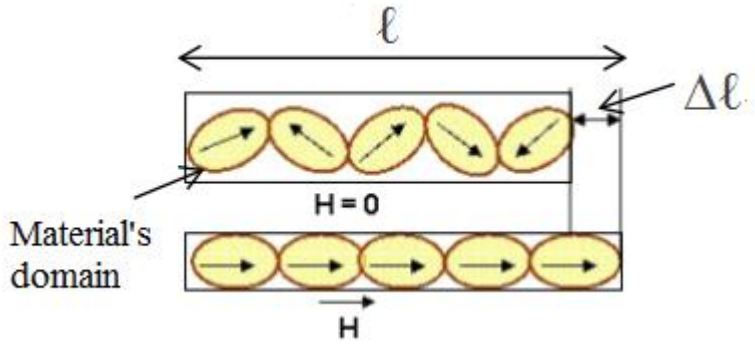

Figure 2.2: *Magnetostriction and domain walls rearrangement in ferromagnetic materials under applied magnetic field.*

Figure 2.2 shows that the electron clouds of ferromagnetic material remain scattered in the absence of magnetic field *H*. Applied magnetic field moves the domain walls where electron clouds rearrange to align in the direction of the magnetic field. The change in the length is measured as a function of strain λ expressed as $\Delta\ell/\ell$ which is measured in micro meters. Strain can either be positive or negative, where positive strain increases the length of the material and negative strain compresses the material without changing its volume. This is also referred to as positive and negative magnetostriction. At present, various kinds of magnetostrictive materials have been discovered in which rare earth metals terfenol-D and galfenol are quite popular because of large magnetostriction [11], [14] also known as giant magnetostrictive materials. Curie temperature is an important parameter which affects magnetostrictive properties of the material. Curie temperature is also known as the critical temperature which is defined as the temperature at which material loses its magnetic properties. Table 1 classifies different kinds of materials with magnetostriction under specific Curie temperature [14], [11].

Table 2.*1: Comparison of strain capability in different magnetostrictive materials*

MATERIAL	MAGNETOSTRICTIVE CONSTANT (10^{-6})	CURIE TEMPERATURE (K)
Fe	-14	1040
Ni	-50	630
Co	-93	1393
Fe_3O_4	60	860
$TbFe_2$	2630	643
Metglass 2605s	60	370
Terfenol-D	2000	650
$Tb_{0.5}Dy_xZn$	5000	200
$Tb_{0.5}Zn_{0.5}$	5500	180

Also, magnetostriction differs for different materials due to change in magnetic anisotropy. Because of anisotropic nature the material shows difference in magnetostriction for forces acting in longitudinal direction and transverse direction [13].

According to [13], all ferromagnetic materials cannot provide high rate of change of magnetic flux because of low magnetostrain. Studies show that rare earth metals such as terfenol-D, $Tb_{0.5}Zn_{0.5}$ and $Tb_{0.5}Dy_xZn$ exhibits higher magnetostriction making them attractive for energy harvesting applications [15]. However, terfenol-D is the most commonly used material in energy harvesting applications because of its high magneto-mechanical coupling coefficient, higher Young's modulus and large saturation magnetostrain as discussed in [16]. The magneto-mechanical coupling coefficient is the ratio of the two energies (mechanical and magnetic) which determines what part of the mechanical energy is converted into magnetic energy.Vibration based energy harvesting utilizes inverse magnetostriction phenomenon known as Villari effect [17] which is defined as change in the magnetic susceptibility of the material under applied mechanical stress.

2.2.2 Piezo-electric materials

Piezoelectric effect was discovered by two brothers Pierre Curie and Jacques Curie back in 1880. They discovered that electric charge is produced when crystals like tourmaline, topaz or quartz etc. are subjected to mechanical stress. [12]. Their discovery played an important role in the field of photonics, civil and mechanical engineering, microelectronics and biomedical engineering [18]. Piezo-electric materials are very well known and are being employed in many applications like human motion powered generators [4], [2], structural condition monitoring systems [17] and magnetic levitation based energy harvesting etc. [7].

Based on structural characteristics, piezo electric materials are divided into four categories such as ceramics, single crystals, polymers and composite materials (combination of single crystal and ceramics) [19]. Example of ceramic materials is PZT (lead zirconate titanate), for bimorph PVDF (polyvinyldene fluoride) polymer and PMN-PZT (lead magnesium nibolate lead zirconate titante) is for single crystal. The mass density and coupling coefficient for ceramic material PZT-5H is 7.56 g/cm^3 and 0.75 respectively whereas for single crystal (PMN-32PT) the mass density is 8.10 g/cm^3 with high coupling coefficient of 0.95 and the mass density of PVDF composite polymer is 1.78 g/cm^3 with very low coupling coefficient of 0.22 [19], [18].

For energy harvesting application, the mechanical coupling coefficient is very important parameter as the energy density is directly proportional to the coupling coefficient which is further explained in [19] along with the examples.

2.3 Methods of vibration based energy harvesting

The thesis focuses on utilization of ambient vibrational sources for energy harvesting. Various techniques or methods of vibration based energy harvesting involves piezo-electric, electrostatic, electromagnetic and magnetostrictive phenomena. All four methods have their own advantages and limitations. Brief description and working principle of vibrational energy harvesting methods have been discussed along with the examples for proper illustration.

2.3.1 Electrostatic energy harvesting

An electrostatic energy harvesting device uses variable capacitor structure to develop charge due to relative motion between the electrodes of the capacitor with the help of mechanical vibrations as shown in Figure 2.3 [20]. Due to mechanical vibration, the capacitance of variable capacitor changes because of the changing dielectric gap between the fingers (moveable electrode and fixed electrode) as seen from the Figure 2.3.

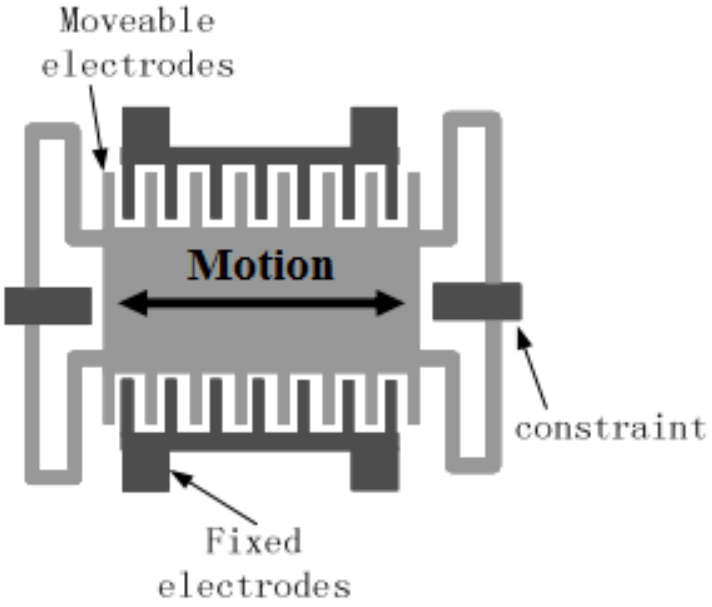

Figure 2.3: *Electrostatic energy harvesting using variable capacitor under horizontal vibration* [20].

The advantages of utilizing this technique includes high voltage output around 2 V to 10 V, possible low cost of the system, and high mechanical coupling coefficient [6], whereas such capacitors may have low capacitance value, µm control of gap between the plates of capacitor and require voltage or charge source during its initialization phase. The energy density of the device can be increased by decreasing the space between the fingers. Furthermore, higher frequency mechanical vibrations seems to reduce the power density of the device which was recorded 0.23 µW/cm^3 at 2.5kHz and 110 µW/cm^3 at 120Hz in [21].

2.3.2 Electromagnetic energy harvesting

Electromagnetic energy harvesting technique follows the basic principle of Faraday's Law where voltage is induced in a pickup coil due to vibrational motion of a moving mass in the magnetic field [22]. The working principle of a spring mass device is shown in Figure 2.4 discussed in [23]. The mass made up of a conducting material is attached to a spring hanging inside the cylinder. A pickup coil is wound inside the cylinder along with a permanent magnet placed at the bottom of the cylinder. Vibrational motion of the mass caused by magnetic attraction and pulling force of the spring induces AC voltage in the pickup coil. The amplitude of induced voltage depends on the displacement distance and the frequency of the vibrations.

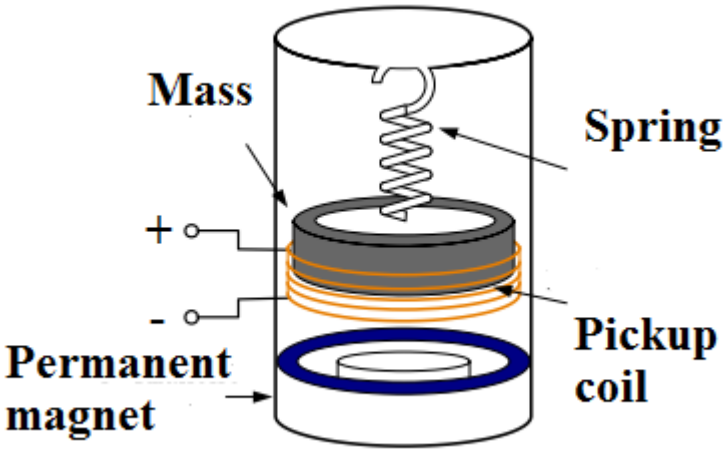

Figure 2.4: *Working principle of an electromagnetic energy harvester* [23].

2.3.3 Thermal energy harvesting

The energy harvesting based on the temperature change of the material utilizing thermo-electric effect is known as thermal energy harvesting technique. Smart materials such as shape memory alloys, piezo-electric and magnetostrictive materials etc. show change in their magnetic properties when heated beyond their Curie temperature [9]. At Curie temperature, material gets demagnetized because of the large change in temperature. The device design usually consists of a cantilever beam and the smart material mounted on beam as shown in Figure 2.5. The mass and a pickup coil is attached at the tip of the cantilever beam. The beam vibrates because of continuous magnetization and demagnetization of the material inducing voltage in the pickup coil placed nearby.

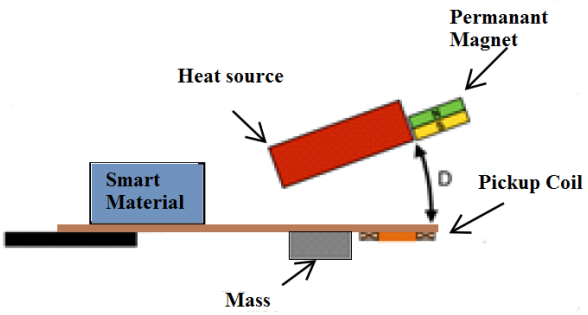

Figure 2.5: *Cantilever based design of thermal energy harvester.*

The amplitude of induced voltage depends upon the frequency of vibrations, the type of material used and placement of the pickup coil as discussed in [9].

2.3.4 Piezo-electric energy harvesting

Piezo-electric energy harvesting technique involves direct actuation of piezo electric material. The strain from mechanical vibration is directly converted to electrical energy. The mechanical coupling coefficient of piezo electric material is comparatively lesser than magnetostrictive materials as discussed in [24]. Piezo electric energy harvesting does not require excitation from external source unlike electrostatic and magnetostrictive energy harvesting techniques. The schematic diagram of piezo electric device is shown in Figure 2.6.

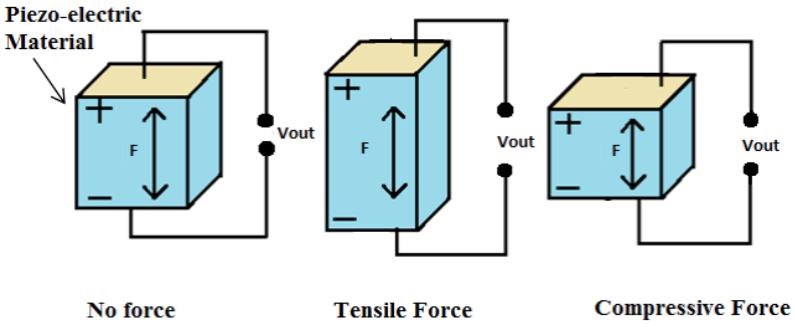

Figure 2.6: *Working principle of piezo-electric transducer.*

A lot of research has been done in the field of energy harvesting utilizing piezo electric transducers under mechanical vibration and many applications have been designed based on piezo-electric generators. Few examples of such applications include energy harvesting from human walking [25], [4], energy harvesting from human breath and limbs in [26] and by damping of mechanical vibrations in civil structures [12] etc.

2.3.5 Magnetostrictive energy harvesting

The inverse magnetostrictive phenomenon is utilized in magnetostrictive energy harvesting (MEH) technique [17]. The inverse magnetostriction also refers to Villari effect which is defined as change in magnetization when the material it subjected to an external stress. Unlike piezo-electric energy harvesting, magnetostrictive material must be magnetized externally either using a permanent magnet or through an excitation coil. The schematic diagram of magnetostrictive energy harvesting is shown in Figure 2.7. The material is first magnetized using permanent magnet and then stressed dynamically using mechanical vibrations. The figure shows the basic working principle of the energy harvester where induced AC voltage is measured across the load.

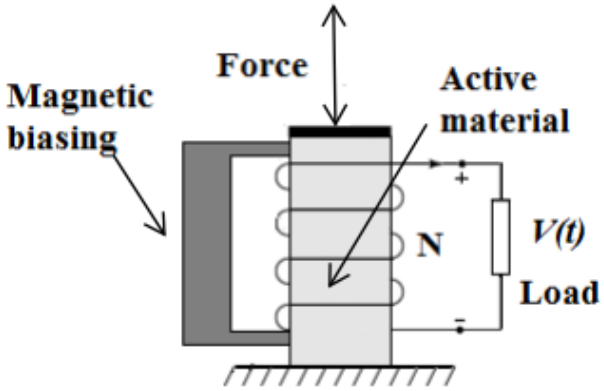

Figure 2.7: *Schematic of magnetostrictive material based energy harvesting device.*

Many applications have been developed so far based on the energy harvested from magnetostrictive materials. The technique has gained its popularity after the discovery of giant magnetostrictive materials (GMM). Dapino in [11] discusses various applications of MEH which includes torque sensors, forces sensors, magnetometers, sonar transducers and linear or rotational motors etc. Structural condition monitoring is another important application for MEH technique as discussed in [27].

2.4 Examples of energy harvesting devices

Based on the above mentioned energy harvesting techniques a comparative study has been done regarding vibration based energy harvesting devices. Examples of various energy harvesting devices have been presented in the upcoming sections followed by a brief discussion regarding their working principle, device design and experimental results. Comparison among devices has been made based on the energy density, maximum output power and feasibility in various applications.

2.4.1 Low frequency high damping electrostatic system

Despesse and Chaillout in [28] have presented a vibrational energy damping device based on electrostatic energy harvesting technique. The harvester was designed to extract power from low frequency vibrations under 100 Hz. Studies show that the frequency of vibrations from ambient vibrational sources like car engine, clothing, dryer, refrigerators, human walking and bridges etc. is below 200 Hz [21], [29]. From existing electrostatic microstructure [30] i.e. (out-of–plain gap closing, in-plane overlap or in-plane gap closing), in-plane-gap closing structure has been utilized due to its maximum capacitance. The schematic of an electrostatic capacitor is shown in Figure 2.8.

It was observed that the harvested power is directly proportional to the mass and relative displacement of moveable and stationary electrodes. The large mass produced larger displacements for the same value of frequency. Simulation has been done for bulk tungsten macrostructure and silicon microstructure at 50 Hz of mechanical vibrations. The results from the simulation showed that the silicon microstructure having a mass of 2 g had maximum displacement of 95 µm producing maximum output power of 70 µW, whereas output power of 6 mW was recorded from tungsten macrostructure of 104 g mass because of the large displacement value of 116 µm.

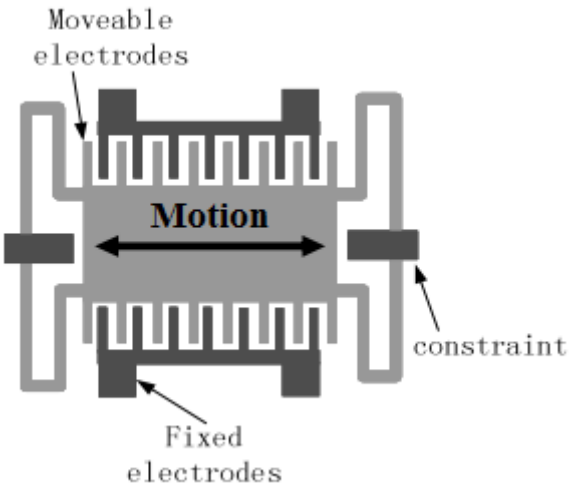

Figure 2.8: *Schematic diagram of electrostatic energy harvester (in-plane gap structure)* [30].

Practical implementation of electrostatic energy harvester was done utilizing tungsten prototype mounted on the engine of a car. The harvested energy was recorded around 250 µW under sinusoidal vibration of 50 Hz causing a displacement of 90 µm. The electric circuit design of an energy harvester is an integral part of the system design process in order to extract reasonable amount of energy from non-linear sources of mechanical vibrations.

2.4.2 Electromagnetic energy harvesting using repulsively stacked multilayer magnets

An electromagnetic energy harvester is proposed in [31] to harvest energy from low frequency vibrations (2 Hz to 8 Hz) from bridges. The conventional single layer electromagnetic energy harvester with single magnet and a pickup coil is shown in Figure 2.9 and the proposed multilayer harvester is given in Figure 2.10. Unlike conventional harvester, the proposed harvester consists of multiple magnets arranged in way that the poles of individual magnets repel each other. Likewise, each magnet in the layer has a pickup coil of its own. The movement of permanent magnet induces voltage in the pickup coil due to

change in magnetic flux density *B*r as shown in both figures. As induced voltage is directly proportion to the frequency of vibration, the multilayer configuration induces more voltage due to the increase in the rate of change of magnetic flux density caused by the use of multilayer magnets and pickup coils.

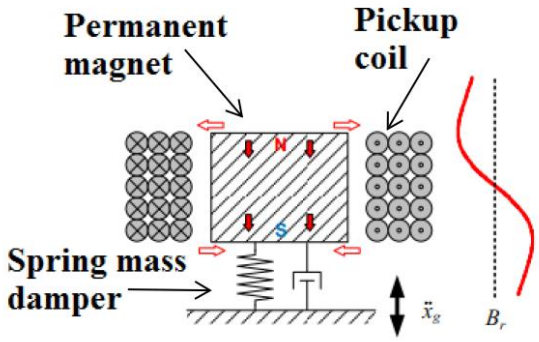

Figure 2.9: *Single layer electromagnet energy harvester.*

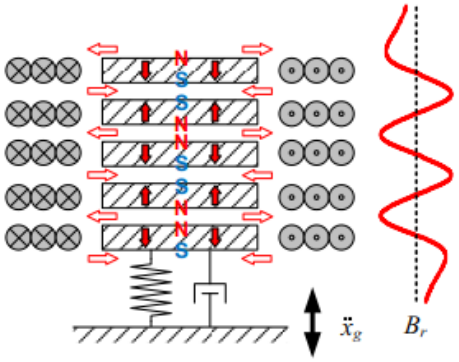

Figure 2.10: *Multilayer electromagnet energy harvester.*

The experimental setup and schematic diagram of the harvester is given in Figure 2.11 where a shaker is used to mimic mechanical vibration measured by an accelerometer [31]. Two sets of coils were utilized having 980 turns in coil 1 and 1960 turns in coil 2 both attached to the actuator below the proof mass as shown in Figure 2.11 below.

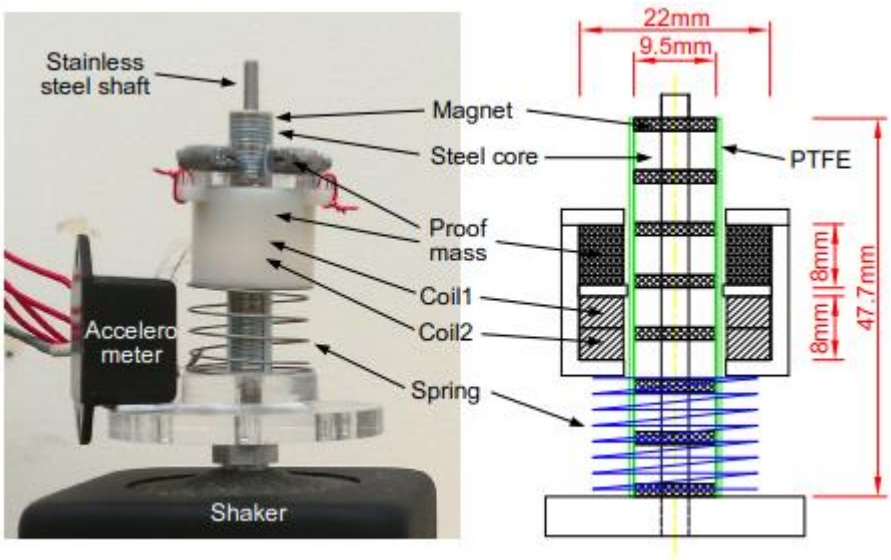

Figure 2.11: *Prototype device for electromagnetic energy harvester* [31]**.**

The output voltage is measured by changing the load resistance and the optimal value was calculated to be 680 Ω producing 2 V_{PP} and peak power of 3.8 mW for both the coils.

The experimental results showed that the average output power of 0.12 mW can be harvested when repulsively stacked multilayer magnets vibrate with the frequency of 4.95 Hz.

2.4.3 Thermal energy harvester based on magnetic shape memory alloy

Magnetic shape memory alloy (MSMA) also known as smart material show large change in their magnetization characteristics below Curie temperature. Studies show that MSMA offers 10% more strain as compared classic shape memory alloy SMA making them attractive for energy harvesting applications as discussed in [32].

- **Device design and working principle**

The working principle of MSMAs involves temperature dependent magnetization change which results in mechanical vibration producing energy [9]. Advance research in material sciences and technology has made it possible to design multi-ferric MSMA materials having low hysteresis loss and high permeability [32]. The magnetization of the alloy changes abruptly when it is subjected to heat a source. The recovery phase for such alloy is quite fast after being released by heat source. Due to high heat transfer rate and fast recovery, such materials have high cycling frequencies making them good for the energy harvesting application at miniature scale [9], [33]. Ni-Co-Mn-Ga films were used as an active material in the harvester because of having special characteristics like low Curie temperature i.e. (150 ^{o}C) and large strain values [9].

The working principle of the proposed thermal energy harvester is shown in Figure 2.12. The micro actuator consists of magnetic shape memory alloy cantilever as an active material along with an integrated pickup coil attached at the tip of the cantilever. The micro actuator is aligned with respect to a tiny magnet attached at front of the heat source. The cantilever can freely vibrate due to continuous magnetization and demagnetization of the active material.

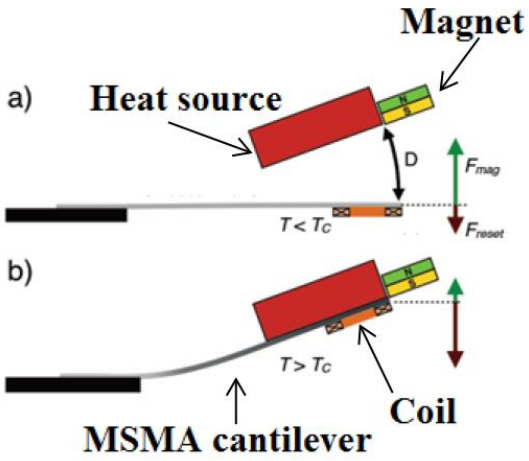

Figure 2.12: *Principle of operation in MSMA based energy harvesting device in* [9].

The working principle of the harvester is explained in two phases. In phase "a", below Curie temperature T<Tc, the material is deflected towards the heat source because of the force of attrition between permanent magnet and cantilever. When cantilever touches the heat source, the material changes its magnetic property due to change in the temperature and performs transition from ferromagnetic state to paramagnetic state. The material gets demagnetized when temperature exceed its Curie temperature Tc>T shown in phase "b". The cantilever detaches and the initial properties of the material restores. This cycle continues allowing cantilever to vibrate causing change in the magnetic flux and induces voltage in the pickup coil.

- **Experimental results**

Experimental results showed that the proposed device can harvest 0.12 µW of power with the peak current value of 100 µA when the cantilever is vibrating at 100 Hz [9]. The number of turns used for the pickup coil is 100. The optimal value of power was obtained by the method of impedance matching. The energy density of the device was reported to be 3 mW/cm^3 for the temperature change of 2 K. It was concluded that the harvested power depends on the distance between the cantilever and heat source. The larger the distance the higher will be the amplitude of vibrations and consequently higher power levels.

2.4.4 Magneto-electric composite based energy harvesting devices

Comparison between magnetostrictive and piezo-electric materials in [24] show that the energy density of magnetostrictive materials is relatively high as compared to piezo electric materials. Thus, high power density can be achieved when both magnetostrictive and

piezo electrical materials are coupled together forming a magneto-electric laminate composite. By applying magnetic field externally, magnetostrictive material will undergo deformation. As both magnetostrictive and piezo electric materials are coupled, deformation in magnetostrictive material will cause actuation of PZT material developing electric charge across piezo-electric material.

a) Vibrational energy harvesting using magnetic levitation

Energy harvesting device consists of piezo electric material PZT sandwiched between layers of strong magnetostrictive material terfenol-D forming magneto-electric composite material. Energy is harvested utilizing low frequency nonlinear vibrations created by magnetic levitation.

- **Mechanical design and working principle**

The proposed energy harvesting device and its working principle is shown in Figure 2.13 [7]. The device consists of three permanent magnets attached to a pipe. Both top and bottom magnets are fixed whereas the middle magnet can move freely due to the magnetic levitation created by the pole placement of the top and bottom fixed magnets.

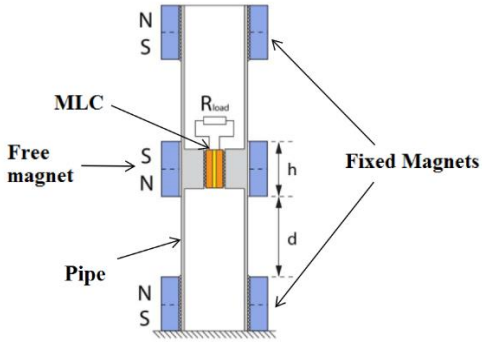

Figure 2.13: *Structure and working principle of the harvesting device* [7].

The middle magnet consists of magneto-electric laminate composite (MLC) and the pickup coil located inside the pipe. A load resistor is attached to the coil for measuring the output power. The middle magnet undergoes non-linear oscillations when the device is subjected to external vibrations. The non-linear oscillation of middle magnet creates changing magnetic flux around the magneto-electric laminate shown in Figure 2.13.

MLC consists of a PZT layer sandwiched between layers of terfenol-D as seen from Figure 2.14. Strong bond is made between PZT layer and terfenol-D so that mechanical strain transfers easily across the layers. Changing magnetic field causes magnetostriction allowing terfenol-D to expand and contract respectively. Because of strong coupling among the layers, expansion and contraction of magnetostrictive material allows PZT layer to expand and contract simultaneously. The oscillation of central magnet induces voltage in the pickup coil.

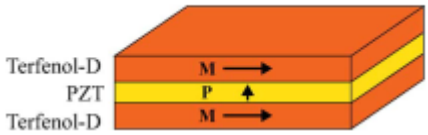

***Figure 2.14**: Magneto-electric laminate composed of PTZ layer sandwiched between layers of Terfenol-D* [7].

- **Experimental results**

During the experiment, harmonic based excitation at 10 Hz with the mass of 1 g was applied to magneto-electric laminate composite (MLC) attached with the middle magnet. It was observed that the relative displacement of central magnet depends upon the distance between top and bottom magnets and the amplitude of harmonic based excitation. The waveform of displacement is shown in Figure 2.15 whereas the open circuit voltage developed across pickup coil is given in Figure 2.16.

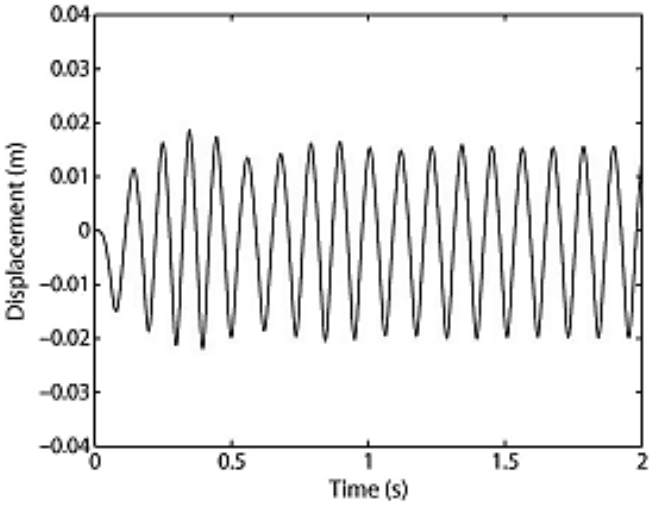

***Figure 2.15:** Central magnet's relative displacement under harmonic based excitation* [7].

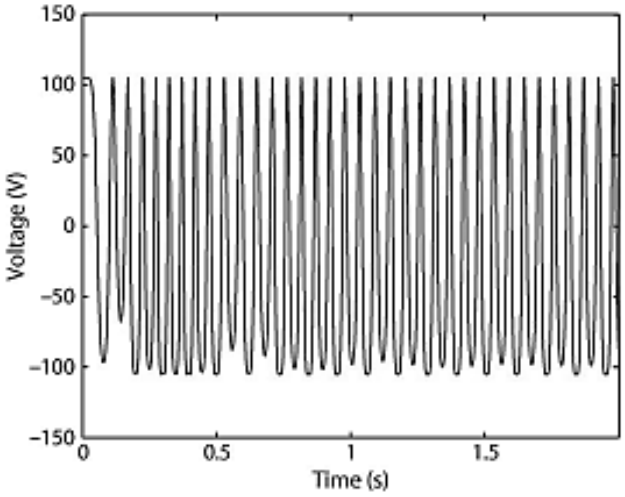

Figure 2.16: *peak to peak voltage at 10Hz* [7].

The peak value of output voltage can be seen from the Figure 2.16 which is nearly 100 V but frequency of the voltage signal is twice as the frequency of displacement signal. Output power was reported up to maximum of 1.1 mW using $10x10^6\ \Omega$ resister [7]. The results show that due to the strong mechanical coupling, the energy density of MLC is 3.48 W/m^3 which is quite large as compared to the thermal energy harvesting technique proposed in [9].

b) High power density magneto-electric energy harvester

The energy harvesting device proposed in [34] can harvest energy either by piezo-electric or magnetostrictive phenomena. Piezo-electric and magnetostrictive laminates offer high power density, thus increasing the energy harvesting capabilities of the vibration based energy harvester.

- **Device design and working principle**

The proposed energy harvesting device and its components are given in Figure 2.17 [34]. Two piezo electric fibers $Pb(Zr,Ti)O_3$ with multi symmetric polarization for longitudinal and bending vibration are coupled with four layers of FeBSiC ferromagnetic material. Output is taken as a voltage difference across V_A and V_B. Induced voltage is the outcome of piezo electric effect triggered either by direct impact or by externally applying the magnetic field utilizing magnetostrictive phenomena resulting in vibrations.

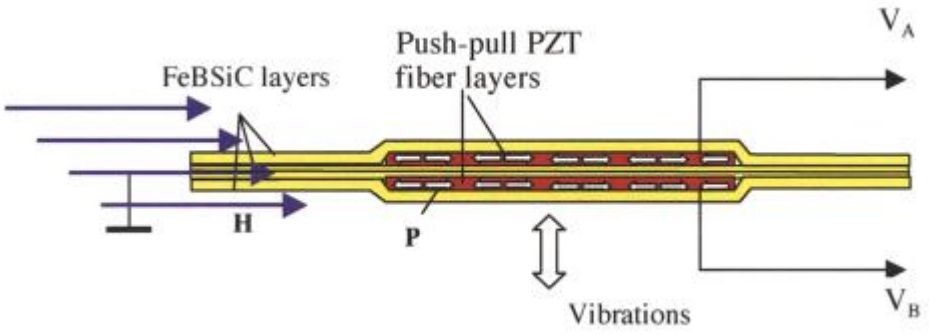

Figure 2.17: *Magneto electric energy harvesting device* [34].

- **Experimental results**

Experiments were performed using both mechanical vibrations and by applied magnetic field. The harvester is first mechanically stressed at 21 kHz frequency resulting in the output power of 429 µW/Oe as shown in Figure 2.18 where (1 Oe = 78.57 A/m). In second set of experiment the magnetostrictive material is magnetized using AC magnetization of 1 Oe resulting in the induced voltage of 63 V_{PP}/Oe producing peak output power of 420 µW/Oe. The harvester was then tuned to achieve power density of 400 µW/g-cm^{-3} by changing the stiffness of the structure and using low frequency mechanical vibrations of 40 Hz.

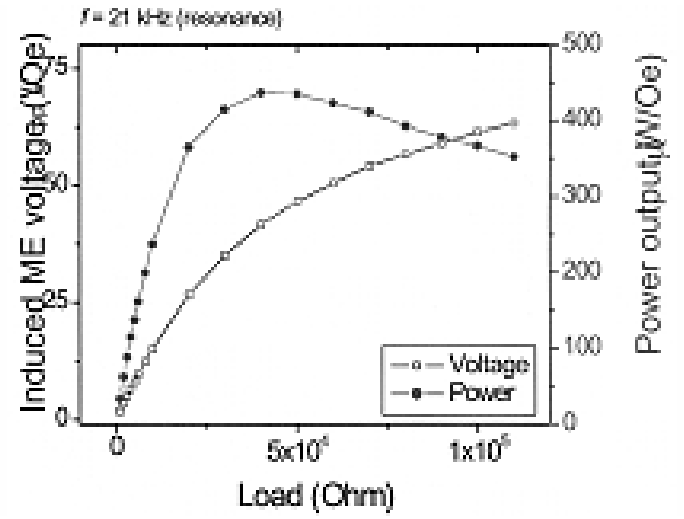

Figure 2.18: *Energy harvested using magnetic field* [34].

2.4.5 Low frequency piezo-electric energy harvester

Human motion is subjected to low frequency vibrations, for example, the step frequency of human walking is only 1 Hz [4]. Energy can be harvested by variety of ways from human body which is thoroughly discussed by T. Starner in [26]. Harvested energy from body organs can be used to power health monitoring devices or wearable body implants

[2]. Studies show that a person walking 2 steps per second weighing 68 kg can theoretically produce 67 W of power. Practically, due to loss of mechanical power by the effect of gait, a lot less power can be scavenged as compared to the ideal case. Studies show that 75% of mechanical power is lost during energy transformation. Also, taking into account the electrical losses and low coupling of human motion with energy harvesting device, only 1.265 W of energy can be harvested [4], [26].

The first energy harvesting device based on piezo-electric material was fabricated by researchers of MIT, where a sole mounted PVDF laminate based energy harvester was designed as discussed in [4]. Shenck and Paeadiso in [25], [35] utilized bimorph PZT material to harvest energy from heal strike. Impact based energy harvesting concept utilizing piezo-electric is proposed by Renaud et al. in [36]. Molding and design of a piezo-electric energy harvester using vibrations from road traffic is proposed by Zhiwei and Hongjun in [37], where the results for output power were predicted for different loads of vehicles moving with different velocities.

The comparison, working principle, and functionality of above mentioned energy harvesting devices are discussed briefly.

a) Polyvinylidene fluoride (PVDF) laminate based harvester

Sole mounted hexagon shaped PVDF laminate based harvester is shown in Figure 2.19. A 2 mm plastic substrate is sandwiched by 8 layers of 28 µm PVDF sheets placed inside sole of the shoe. The device could produce 1.25 mW of power across 250 kΩ resistor when subjected to mechanical vibration of 0.9 Hz.

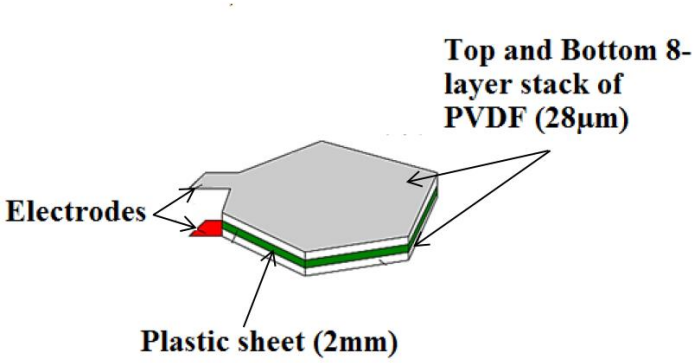

Fugure 2.19: *Polyvinylidene fluoride based energy harvesting laminate* [4].

b) Piezoelectric bimorph based energy harvesting device:

A PZT bimorph is proposed by Shenck and Paeadiso in [25], [35], as shown in Figure 2.20 which was installed in the heels of shoes. The PZT layer was compressively stressed

by the motion of heel deforming the transducer to produce energy. This device could produce 8.4 mW of power under 0.9 Hz of frequency when 500 kΩ resistor is connected across the terminal of the transducer.

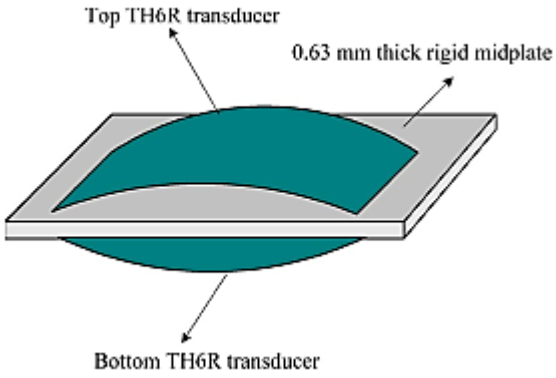

Figure 2.20: *Piezoelectric based bimorph transducer* [4].

c) Inertia based impact coupling type energy harvesting device:

Beside direct straining of piezo-electric material, Renaud et al. in [36] proposed a different concept where he utilized inertia of a moving mass to harvest energy. The harvester consists of a free mass confined in a frame along with piezo-electric cantilever beams at both ends as shown in Figure 2.21. Wrist motion allows mass to slide inside the frame and strike piezoelectric cantilever beam producing energy. The amount of energy harvested depends upon the impact force and acceleration of moving mass. The acceleration of the mass can be increased by attaching magnets on both ends of the frame and metal pieces with the moving mass respectively.

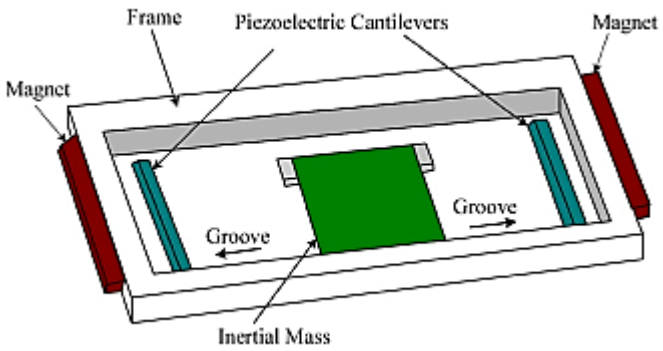

Figure 2.21: *Impact coupling type PZT based energy harvesting device* [4].

This device could produce up to 40 μW of power attached to the wrist moving with the amplitude distance of 10 cm at the frequency of 1 Hz.

In general, all devices presented above are capable of producing power from microwatts to millwatts. On the other hand, output current is quite small as compared to output voltage which makes them non ideal for powering devices that require higher currents.

2.4.6 Magnetostrictive energy harvesting devices

Ferromagnetic material changes its magnetic properties due to the applied stress under magnetic biasing [17]. The magnetostrictive materials have comparatively higher energy density as compared to piezo electric as discussed earlier in [24]. Also, piezo electric materials degrade with time due to stress effects, whereas magnetostrictive materials have longer life span and strong mechanical coupling making them quite ideal for energy harvesting applications [38]. Strong mechanical coupling enables efficient transfer of vibrational energy to actuate the magnetostrictive material. Energy up to watts can be harvested due to the discovery of magnetic shape memory alloys exceptionally strong ferromagnetic materials known as rare earth magnets such as Terfenol and $Tb_{0.5}Dy_xZn$ etc. [15].

a) Magnetostrictive energy harvester based on Villari effect

The energy harvesting device based on the principle of inverse magnetostriction is proposed by Jason Lee in [39]. Magnetic shape memory alloy (MSMA) NiMnCoIn has been utilized as an active material during experimentation. Comparison has been made between NiMnGa single crystal and meta-magnetic SMA (NiMnCoIn) and it was found that energy harvested by meta-magnetic SMA is more for same amplitude and frequency of vibrations.

- **Device design and working principle**

The experimental setup of the device and its different stages are given in Figure 2.22 [39]. The setup consists of an energy harvesting material, rectifier, strain gauge sensor, analog to digital converter and a wireless transmitter. The test material is first magnetized using DC magnetization and then stress dynamically producing changing magnetic flux density. As a result, voltage is induced in the pickup coil wound around the test sample. The AC voltage is then rectified using self-powered four stage rectification and the output voltage is then fed to a wireless sensor. The setup was tested to power up sensors for structural condition monitoring of a bridge.

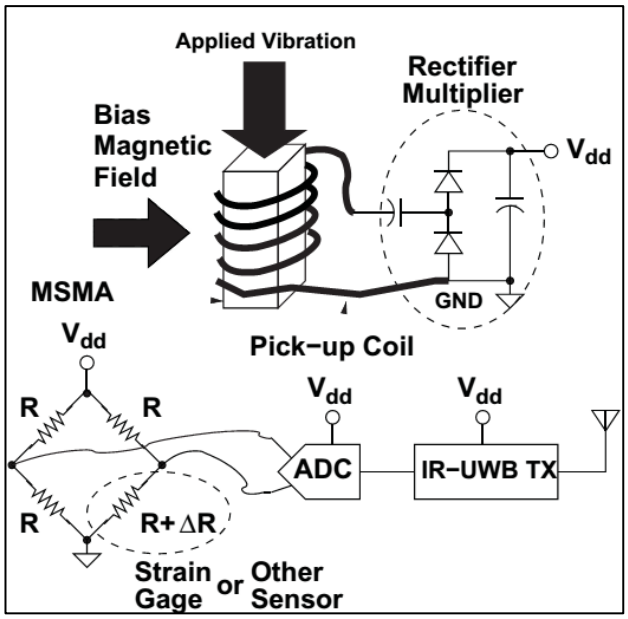

Figure 2.22: *Test setup for energy harvesting using MSMA material and wireless sensor system* [39].

- **Experimental results**

The proposed device produced more than 700 mV DC with the peak input amplitude of 400 $mV_{PP.}$ Single stage bridge rectifier was not useful because of the low output voltage level (400 mV-700 mV), thus, four stage rectification was done to achieve DC level of more than 3 V_{PP} which were sufficient for the operation of wireless sensor. Tests were performed using two different MSMA materials (NiMnGa and NiMnCoIn). The results show that the energy harvested using NiMnCoIn under stress applied parallel to magnetic biasing is more as compared to the stress applied perpendicular to magnetic biasing on NiMnGa sample as shown in Figure 2.23.

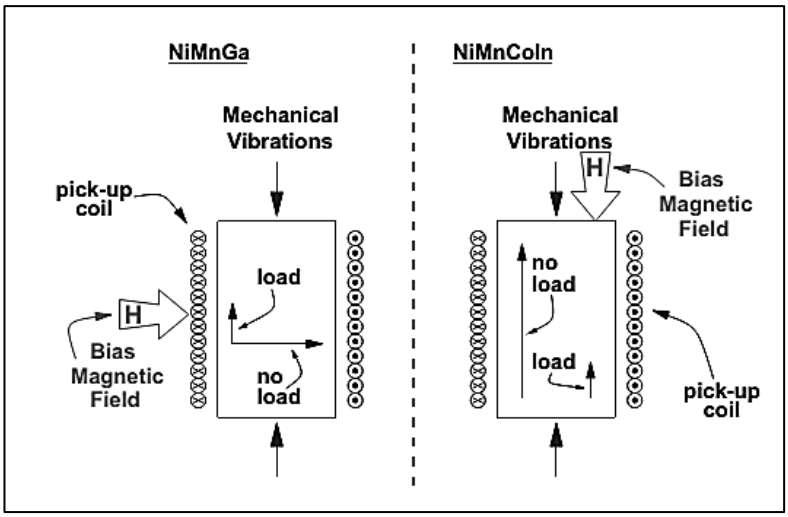

Figure 2.23: *Different methods of magnetic field biasing on test samples under mechanical loading* [39].

It was concluded that increasing mechanical loading frequency or increasing the value of applied stress will result in greater output voltage levels. Experiments were performed using 100 kΩ, 1 MΩ and 10 MΩ load resistors to observe output power levels. The peak power obtained was 100 μW with the DC voltage level up to 3 V_{PP}.

b) Effect of prestress on magnetostrictive energy harvesting under dynamic mechanical vibrations.

The effect of prestress on output power is tested by Zucca in [40]. It was observed that the output power increases when the material is first prestressed and then excited utilizing dynamic vibrations. The details about the modeling of the concept is presented in [41]. The modeling results were tested in [40] with a working prototype device constructed using bulk rod of $Tb_{0.3}Dy_{0.7}Fe_{1.92}$ giant magnetostrictive material . The combined effect of dynamic loading and prestress is observed using two different experimental setups for the sake of comparison.

- **Experimental setup**

The experimental setup is given in Figure 2.24 where the test material is first magnetized using two sets of permanent magnets having magnetic flux of 1.2 T. The active material is compressively prestressed up till the value of sigma_0 = 6.5 MPa with the help of a non-magnetic mechanical frame. Dynamic loading is supplied by a vibrator using different values of stresses at 300 Hz of frequency.

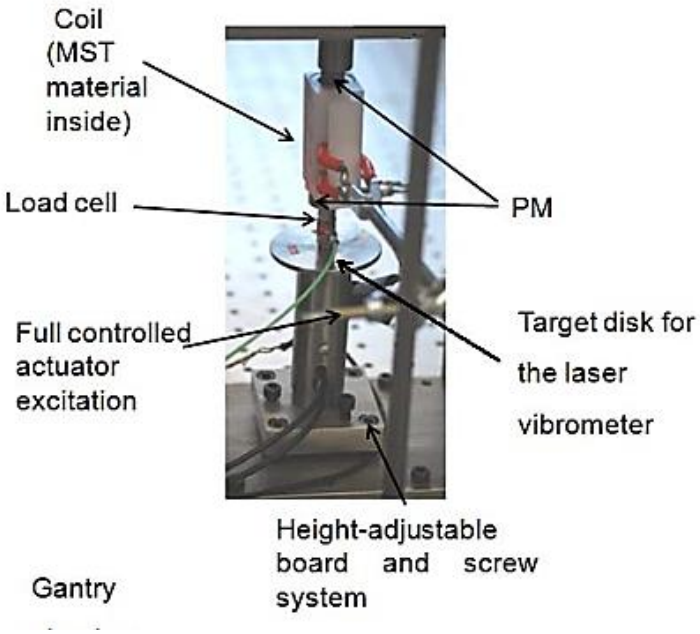

Figure 2.24: *Experimental setup of magnetostrictive energy harvester* [40].

The pickup coil is located inside the test sample, whereas the target disk contains the laser test vibrometer and piezoelectric load cell.

- **Experimental Results**

The experimental results show that maximum output power of 82.8 mW can be harvested when the amplitude of vibration is close to the prestress value. The power density was measured to be 5.2 mW/cm^3 for the harvester. It was concluded that increasing the frequency of vibration also increases the output power until it reaches at saturation level. Likewise, increasing the amplitude of vibrations increases the output power but it should not exceed from the prestress value to avoid noise in the output signal and structural damage. Also, it was observed that increasing the number of turns does not increase the output power linearly. The results from different sets of coils are given in Table 2 where material is compressively preloaded at σ_0 = 6 MPa under dynamic stress of σ_{0pk} = 0.82 MPa.

Table 2.2: *Coil design parameters effecting output power* [40].

Coil	**Turn number**	***P*** **(mW)**	I_{rms} **(mA)**	R_M **(Ω)**	**Wire diameter (mm)**
1	288	2.2	33.2	2.0	1.0
2	540	3.0	20.7	7.0	0.5
3	990	3.8	11.3	30.0	0.5
4	24300	4.2	0.53	15000	0.1

3. VIBRATION BASED ENERGY HARVESTING APPLICATIONS

The concept of energy harvesting from ambient vibrations has been discussed in Chapter 2 where introduction about various techniques of vibration based energy harvesting has been presented. The term energy harvesting or energy scavenging refers to the designing an actuating device for small scale power production and developing an energy storage system. The question regarding the need for energy harvesting devices has been answered in this Chapter by discussing various applications developed so far. The energy harvested from ambient vibrations will allow maintenance and battery free operation of small scale power electronic devices, sensors and actuators. The applications are strongly depended on the amplitude and frequency of vibrations. The harvested energy is usually quite small (miliwatts or microwatts) demanding careful design of the energy extracting circuitry.

Among all techniques, piezo-electric and magnetostrictive energy harvesting is very well developed and thus most of the applications are designed based on piezo-electric and magnetostrictive materials. The number of applications have increased quite a lot due to the discovery of thin film PZT materials, piezo-electric bimorphs, giant magnetostrictive materials and magnetic shape memory alloys. Few such applications have been discussed in this chapter related to structural condition monitoring, wearable body implants, sonar transducers, powering wireless sensor nodes, position and forces sensors etc. The details regarding the employed smart material and working principle of the harvester is also presented for each application in later sections.

3.1 Powering wireless sensor nodes

Vibration based energy harvesting is primarily employed for powering ultra-low power wireless sensors nodes and micro actuators. The sensors and actuators can be utilized for monitoring purposes as discussed by Mitcheson in [2]. The need for continuous monitoring of human health (blood pressure, breathing and hart rate monitoring), civil structures and mechanical wear and tear demands sensors to be autonomous in terms of power requirements. Studies in [42] are related to various energy harvesters that have been designed and implemented successfully which includes body-mounted and implanted medical devices, energy harvesting from heel strokes, vibrations from car engine and kinetic energy harvesting form human motion etc.

The power requirement for basic wireless sensor system for temperature measurement is presented in article [2]. The wireless system consists of various modules having different power requirements. For example, temperature sensor require 12 μW, ADC (analogue to

digital converter) and transmitter require 1 µW and 0.65 nW, respectively, for their operation [43]. The power could be supplied by the energy captured from human motion. However, due to the fact that the harvested energy from vibrational sources is in mW and µW the power consumption for various applications is considered before supplying energy from the harvester. As an example, radio frequency tags require 250 µW whereas calling operation of a mobile phone require 1.7 W and pager require 0.030 W of power for their operation. The energy harvested from human motion is reported 0.903 W in [1] which is sufficient to supple power to pagers and RF tags etc.

3.2 Self-powered body mounted and wearable body implant

The irregular vibration from human body are promising candidates for self-powered body-mounted biomedical electronics and wearable implants. The research related to wearable body implants is more focused towards utilization of highly efficient piezo-electric materials and many applications have been developed in this regard. Study regarding energy harvested from the organs of human body has been presented by Starner in [26] where he proposed a theoretical way of calculating the potential energy that can be harvested using motion of human organs. Starner presented various potential ways of energy harvesting from human body including breath, blood pressure, upper limbs motion, walking and body heat. The theoretical calculations show that the available power from the human breathing mechanism, blood pressure and limb motion is nearly 1 W, 0.93 W and 35 W respective which is enough to power mobile devices and electronic devices consuming low power.

A working prototype of self-powered cardiac pacemaker is proposed in [44]. The input current and voltage requirement for the operation of the pacemaker is 100 µA and 3 V respectively [45] demanding utilization of highly efficient energy harvesting material. The proposed harvester is constructed by single crystalline piezo-electric PMN-PT thin film which can produce 4 times higher charge as compared to the conventional PZT [46]. The maximum output current and voltage for the harvester were reported 145 µA and 8.2 V respectively with the peak current value of 223 µA. The bending movement of the harvester causes direct pacemaking as shown in Figure 3.1 [44].

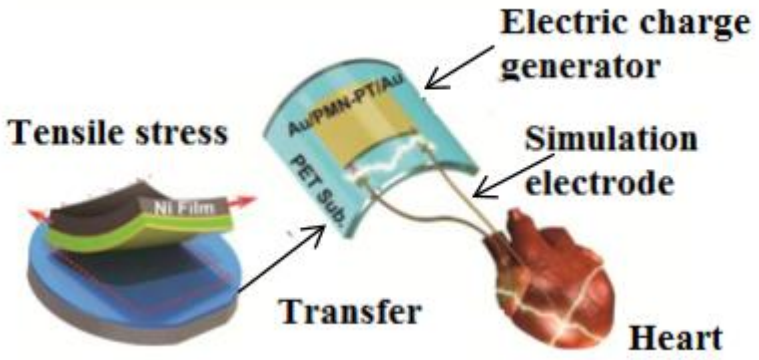

Figure 3.1: *Piezo-electric based pacemaker device* [44].

3.3 Structural condition monitoring

Structural condition monitoring is another important application of vibration based energy harvesting. Currently structural condition monitoring is being carried out using wireless sensors nodes and actuators. Non-destructive evaluation of structural damage is presented in [47] where a coil is placed inside the concrete structure and impedance of the coil is measured before and after the damage in the structure. Change in the impedance of the coil was noticed due to damage in the concrete section. Another technique of monitoring structural condition is presented in [48] where the natural frequency of bridge vibration is calculated. It was observed that the natural frequency of bridge vibration changes because of damage in the bridge structure. In [49] the author has presented a wireless sensing system for structural condition monitoring which includes RFID (radio frequency identification) tags and readers. The tags were embedded inside the structure sending the information of strain gauge sensor to RFID reader.

The developed techniques for structural condition monitoring require reliable and continuous source of power supply. The vibrational based energy harvesting techniques can be utilized to supply power to condition monitoring systems, wireless sensors and actuating devices [39]. In [31] the author has proposed an electromagnetic generator with repulsively stacked magnetics to harvest energy from low frequency bridge vibrations. The average power of 0.12 mW was harvested which could then be supplied to wireless sensing nodes for their operation. Another device is proposed in [50] utilizing magnetic shape memory alloy to harvest energy from mechanical vibrations in bridges. The device could provide peak power of 100 µW with the voltage of 3 V_{PP} which is enough to power an RFID tag to collect information from the strain gauge. Also, the design of electrical circuitry plays a key role to efficiently extract energy from mechanical vibrations. Energy harvesting from pavements of road is investigated in [37] utilizing piezo-electric material embedded 5 m below the road. The straining of piezo-electric transducer is caused by moving traffic on the road. It was suggested that theoretically 200 kW of power can be

harvested theoretically utilizing this technique from 1 km road embedded with piezo-electric transducers.

3.4 Sonar transducer

Terfenol-D is the most widely used giant magnetostrictive material employed in making actuators and transducers. Terfenol-D is popular because of its ability to withstand high strain values having higher Young's modulus, broad frequency range and higher energy density as compared to other magnetostrictive and piezo-electric materials [11].

It is often required that sonar transducers should be able to operate at low frequencies producing high mechanical power at broad bandwidth. Nickel was popular material to be used in making sonar applications during 1939 [51]. Because of low magneto-mechanical coupling coefficient (k= 0.3) of nickel, high power output can only be achieved by keeping high quality factor *Q.* Discovery of giant magnetostrictive materials made it possible to work at broader frequency range and lower quality factor because of having exceptionally good material properties including high energy density, large strain values and strong magneto-mechanical coupling [11], [52]. The comparison of the material properties between giant magnetostrictive material (terfenol-D) and piezo-electric material PZT [52], [24] is given in Table 3. According to [52] giant magnetostrictive material Terfenol-D can be used to manufacture high power - low frequency sonar transducer and the strain capability of the material is way better than piezoelectric material allowing it to attain higher output power even at low frequencies.

Table 3.1: *Material property comparison among Terfenol-D and PZT.*

Property	**Terfenol-D**	**Piezo electric**
Saturation strain	$1500x10^{-6} – 2000x10^{-6}$	$100x10^{-6}$
Coupling coefficient	0.7 – 0.8	0.3 – 0.65
Energy density (kg/m^3)	$5x10^3 – 25x10^3$	$3.5x10^3$
Sound velocity (m/s)	1395 – 2444	3500
Frequency range	DC to kHz	kHz – MHz
Curie temperature (°C)	357	300 – 370

3.5 Energy harvesting through damping of vibrations

Mechanical vibration exists almost everywhere especially in large rotating machines such as turbines, hydraulic machines and motors etc. Consistent vibration from such machines pose threat to civil structures, thus a damping system is required to reduce the impact of

such vibration. Magnetostrictive materials can also be utilized as a damping device producing electrical energy as a result. Thus, electrical energy can be harvested from vibrations otherwise wasted giving twofold advantages.

Zhangxian and Vivake proposed a vibration ring to damp vibrations caused by the driveline of a motor in [53]. The ring consists of rods made up of giant magnetostrictive material. Experiments were carried out using Galfenol and Terfenol-D rods and the results were compared in terms of power harvested and loss factor as discussed in [53]. The mechanical setup is shown below in Figure 3.2. Each rod consists of a pickup coil and permanent magnets acting as an external magnetic excitation source.

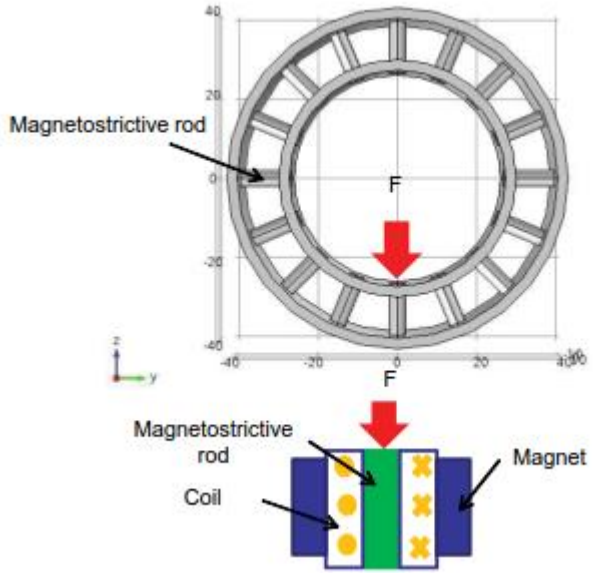

Figure 3.2: *Vibration ring and energy harvesting device setup* [53].

Different values of capacitive and resistive loads were used to track the maximum power point of the proposed system. The power levels of 0.58 W and 0.21 W were obtained from Galfenol and Terfenol rods respectively, under 280 N force at vibrational frequency of 750 Hz.

3.6 High pressure pump based on magnetostrictive material

The phenomena of magnetostriction can also be incorporated in applications like hydraulic systems as described in [54]. Excellent properties of Terfenol-D allow its integration in a high pressure hydraulic pump. Comparing other active materials, magnetic strain of Terfenol-D is very high (2000 ppm) along with strong magneto-mechanical coupling [24]. The high pressure pump device is given in Figure 3.3 below.

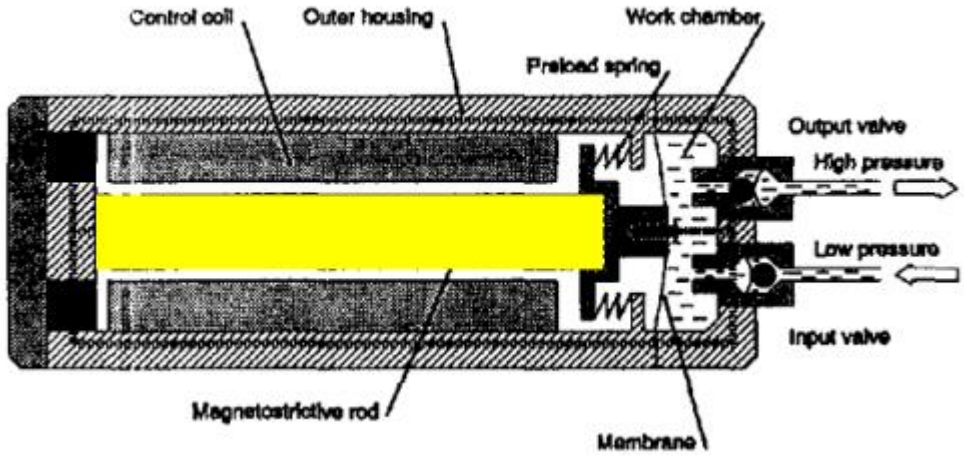

Figure 3.3: *Magnetostrictive material based high pressure fluid pump* [24].

The device consists of a magnetostrictive rod and an external excitation coil along with high pressure and low pressure valves. When external voltage is applied to the coil, the magnetostrictive material gets magnetized and the strain in the material causes increase in the length of the rod. Small strokes due to magnetostrictive phenomena build fluid pressure inside the chamber. The proposed device can build pressure up to 4.2 MPa with fluid flow rate of 3 l/min [15], [54].

3.7 Deformation and position sensors

A strain gauge sensor using transverse-field annealed magnetostrictive ribbons has been made from Metglas 2605SC as discussed in [11]. Change in the permeability of the material is caused by the strain which is sensed by the magnetostrictive material. The gauge factor F_g of the magnetostrictive material based strain gauge was calculated to be about 250,000 which is a lot more than semiconductor gauge factor ($F_g = 250$). The position sensing device is made up of a magnetostrictive material acting as an acoustic waveguide [11]. The device consists of a moving permanent magnet which moves along the magnetostrictive waveguide, an emitter/receiver head on one end for sending the current pulses down to the waveguide and a damper at the other end to avoid unwanted wave reflections as shown in Figure 3.4. The position sensor device can be used to sense the fluid level when moveable magnet is connected to a float.

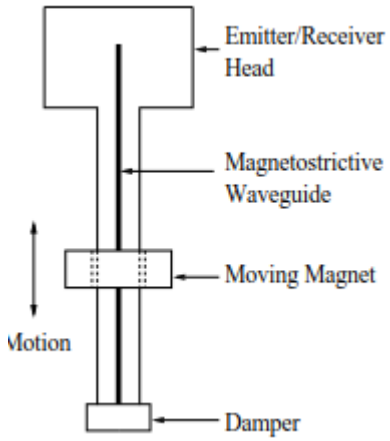

Figure 3.4: *position sensor based on magnetostrictive waveguide* [11].

4. DEVICE DESIGN AND WORKING PRINCIPLE

From the literature review presented in Chapter 2, it became quite evident that magnetostrictive materials have high magneto-mechanical coupling (k > 0.9) and can withstand large stress values as compared to piezo electric materials. The magneto-mechanical coupling coefficient is the ratio of the two energies (mechanical and magnetic) which determines what part of the mechanical energy is converted into magnetic energy [55]. The proposed energy harvester was therefore designed based on ferromagnetic material due to the benefits and application explained in Chapter 2 and Chapter 3. Construction steel was utilized as a test sample because of its practical and industrial applications in bridges, buildings and rail tracks etc. This chapter provides the detail overview about the design of the energy harvester and its working principle. The device design includes both mechanical and magnetic circuit design.

4.1 Design objectives

The overall object of the device design involves designing the mechanical grips, test sample and the magnetic circuit, respectively. A brief illustration for each objective is given as follow.

- Determining the dimensions and material of the mechanical grips for holding the test sample. The grips should be able to provide cyclic vibrations to the test sample up till the stress values of +200 MPa to -200 MPa.
- Determining the optimal size and thickness of the test sample made up of sheets of steel joined together in the form of a stack.
- Determining the parameters of the magnetic circuit which includes calculating the dimensions of the core, magnetizing coil and the pickup coil.

4.2 Mechanical design

Mechanical design includes both designing the mechanical grips and the test sample. The design phase started by first selecting the maximum stress value and based on that, the dimensions of test sample and grips were computed. In order to design the test sample, physical properties of construction steel were studied. Buckling was the major concern which had to be considered during the design process. Calculation for the design parameters of the test sample and mechanical grips are given in the upcoming sections. The design parameters of mechanical grips depend upon the design parameters for the test sample whereas the design parameters of the test sample were calculated for the maximum stress values keeping in view the buckling load.

4.2.1 Test sample design

Three different test samples of construction steel were designed and tested to compute the magnetization curves. In order to apply compressive stress up till 200 MPa, buckling load was calculated to determine the effective length of the test sample. The effective length is the maximum length of the test sample upon which mechanical stress is to be applied. Buckling phenomena is explained briefly for different end fixing cases.

- **Buckling in columns**

Buckling load or critical load is defined as the maximum axial compressive load applied to a column at which the structure can no longer support the load and starts bending. Buckling load depends upon the shape, cross sectional area and length of the column. In order to calculate critical buckling load, formula developed by Euler and Johnson can be utilized based on the length of the column. The calculations do not take non-idealities and eccentricities of load and thus the calculated load is theoretical. Buckling load for long column is calculated using Euler's formula [56] whereas buckling load for short column is calculated by using Johnson's formula [57]. The effective length L_e (4.1) of the column depends upon the end support condition K (pinned, fixed and free) also sometimes referred to as end boundary condition. The effective length is given as

$$L_e = KL, \tag{4.1}$$

where K is the end support constant and L is the length of the column. Different scenarios of end boundary conditions are shown in Figure 4.1. The theoretical values of K are mentioned in the figure whereas the practical values were taken to be K = 1 for (Pinned-Pinned), K = 0.65 for (Fixed-Fixed), K = 2.1 for (Free-Fixed) and K = 0.8 for (Pinned-Fixed) end support conditions, respectively [57].

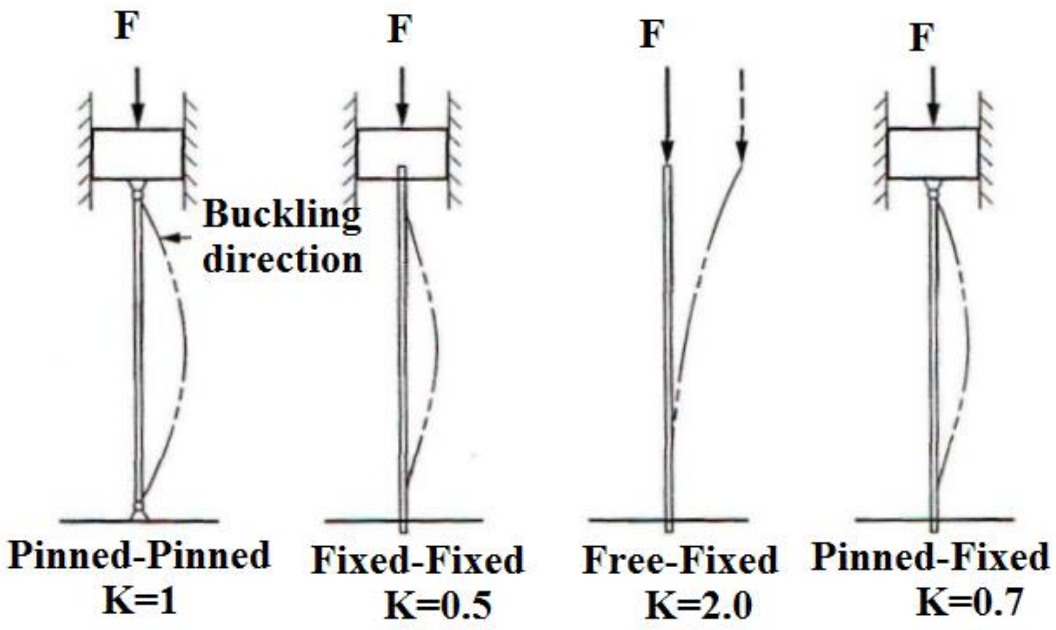

Figure 4.1: *Buckling for different end support conditions* [57].

- **Calculation for buckling load**

The calculation for buckling load is presented in [56] and [57]. Buckling load calculation first involves calculating the radius of gyration *R* (4.2) which is the ratio of area moment of inertia (4.3) and the cross sectional area *A* of the column. Area moment of inertia determines the axis of the bending movement upon buckling and usually taken as minimum values which is calculated for rectangular columns as

$$R = \sqrt{\frac{I}{A}}, \tag{4.2}$$

$$I = \frac{bh^3}{12}, \tag{4.3}$$

where *b* and *h* are the height and width of the column. After calculating *R*, the slenderness ratio λ (4.4) and column constant *C* (4.5) are calculated in order to classify the column type as [57]

$$\lambda = \frac{L \times K}{\sqrt{\frac{I}{A}}}, \tag{4.4}$$

$$C = \sqrt{\frac{2\pi^2 E}{\sigma_y}}, \tag{4.5}$$

where L is the length of the column, A is cross-sectional area, K refers to end support constant, E is modulus of elasticity and σ_y is the yield strength of the column material. The length of the column is determined by its slenderness ratio. For structural steel, the column is considered to be short if λ is less than 40, whereas for the intermediate column λ is between 40 to 150 and for long columns the λ is greater than 150 respectively [58].

Based on the type of column (short, medium and long), Euler's and Johnson's formula can be utilized to calculate the buckling load denoted by F_{Cr} in (4.6) and (4.7) as [58]

$$F_{\mathrm{Cr}} = A\sigma_{\mathrm{y}}\left(1-\frac{\sigma_{\mathrm{y}}\dfrac{KL}{R^2}}{4\pi^2 E}\right) \tag{4.6}$$

$$F_{\mathrm{Cr}} = A\sigma_{\mathrm{y}}\left(1-\frac{\left(\sigma_{\mathrm{y}}\dfrac{KL}{\sqrt{I/A}}\right)^2}{4\pi E}\right) \tag{4.7}$$

The hydraulic press machine was utilized to apply mechanical stress on to the test sample. The end fixing condition for the application of cyclic vibration was considered to be fixed-fixed as both ends of the test sample were attached to the mechanical grips which will be presented in later section of device design. Studies show that the shape of column strongly affects the buckling load [56]. A rectangular shaped column will more likely to be buckled in the direction of the longest length whereas a square shaped column can bear more load thus buckling will occur at higher values of compressive stress. Based on that, the test sample is designed to have square cross sectional area.

The critical buckling load calculation first involved determining the column length type (short, medium and long) using (4.4) and (4.5) for which I and R were calculated by using (4.2) and (4.3). The free length of the steel bar was set to 100 mm along with the cross sectional area of 400 mm^2. The value of end support constant was taken as K = 0.65 for Fixed-Fixed end boundary condition. Based on the dimensions of the test sample, the slenderness ratio and column constant were computed to be λ = 11.25 and C = 125 respectively. As evident from the calculation, λ < 40 indicates the column length type to be short. Based on the length of the column, Johnson's formula was utilized resulting in the buckling load of F_{Cr} = 90.59 kN or σ_{Cr} = 248 MPa using equation (4.7). The modulus of elasticity and yield strength of the material were taken as E = 200 MPa and σ_Y = 250 MPa during the calculation for buckling load.

The value σ_{Cr} is the maximum compressive stress value that can be applied without buckling. Usually tolerance of 10% is given which means that the applied maximum load

should not exceed 90% of the calculated buckling load. After calculating the dimensions and critical load for the test sample, the results were then utilized to design the mechanical grips. Three different test samples were constructed for experimentation having different plate thickness but the overall dimensions of the test sample were kept constant. Two of the test samples were designed using sheets of steel having thickness of 1.5 mm and 1 mm welded from both ends to form a stack of steel bar with cross-sectional area of 400 mm^2. The third test sample was constructed using a single solid steel bar of 400 mm^2 in order to perform experiments at higher stress values. The overall length of the steel bar was taken to be 345 mm in order to insert the sample into the mechanical grips and the free length of the test sample was kept 100 mm for which buckling load was calculated.

4.2.2 Mechanical grip design

In order to hold the test sample, two sets of mechanical grips were designed which could be fixed to the hydraulic press machine for applying stress. The device design for the harvester was first modelled in AutoCAD utilizing 2D and 3D drawing tools in order to analyse and conceptualize the design before making the actual prototype. Both tensile and compressive forces were to be applied during the experiments, therefore the selection of the material for mechanical grips and its dimensions were chosen carefully. High strength low alloy steel material was utilized to construct mechanical grips because of its low carbon content, high yield strength and resistance to corrosion. The application of the tensile stress demands careful calculations of bolt size and the required torque for tightening the bolts so to firmly hold the test sample for higher values of tensile stress.

The calculation for bolt size and torque is based on the maximum tensile stress value (200 MPa) which was calculated as $T = KDF$, *w*here T represents torque, K is the coefficient of friction (0.2 for dry bolt), D is the diameter of the bolt and F is the axial clamp force. The bolt size was chosen 10 mm and the axial clamp force was calculated from the maximum tensile stress value i.e. 80 kN. Based on the selected diameter of the bolt, coefficient of friction and axial clamp force, the required torque was calculated to be 160 N.mm. The 2D schematic diagram of mechanical grip is given in Figure 4.2.

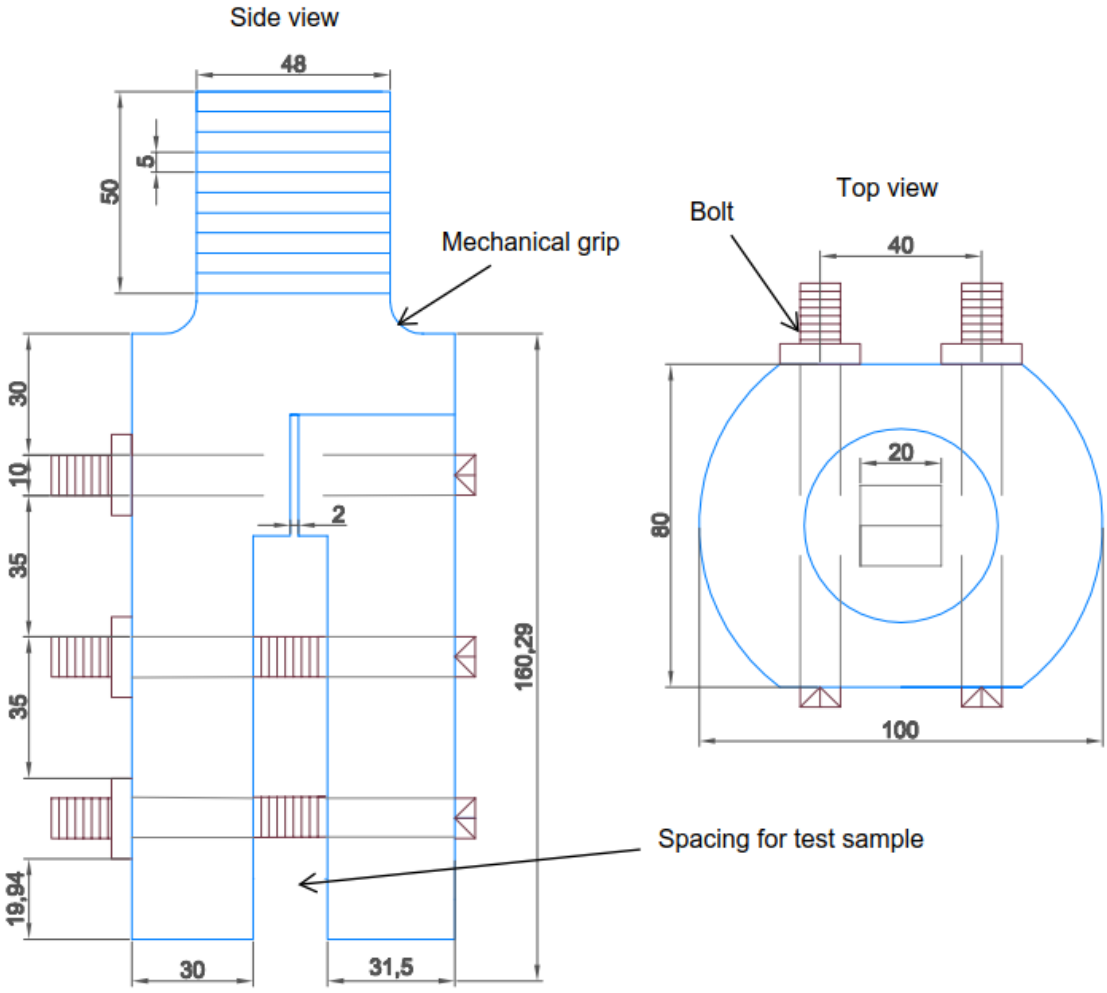

Figure 4.2: *Schematic diagram of the mechanical grip including overall dimensions.*

The 3D model of mechanical grip is given in Figure 4.3. The test sample was fixed inside the spacing of the mechanical grip tightened with the help of 12 bolts. Because of the arrangement of bolts, the required clamp force for holding the test sample was reduced quite much as clamp force exerted by each bolt adds up allowing uniform distribution of the load. Also, the inner surface of the grip was made rough to provide more friction making sure that the test sample would hold firmly by the grips.

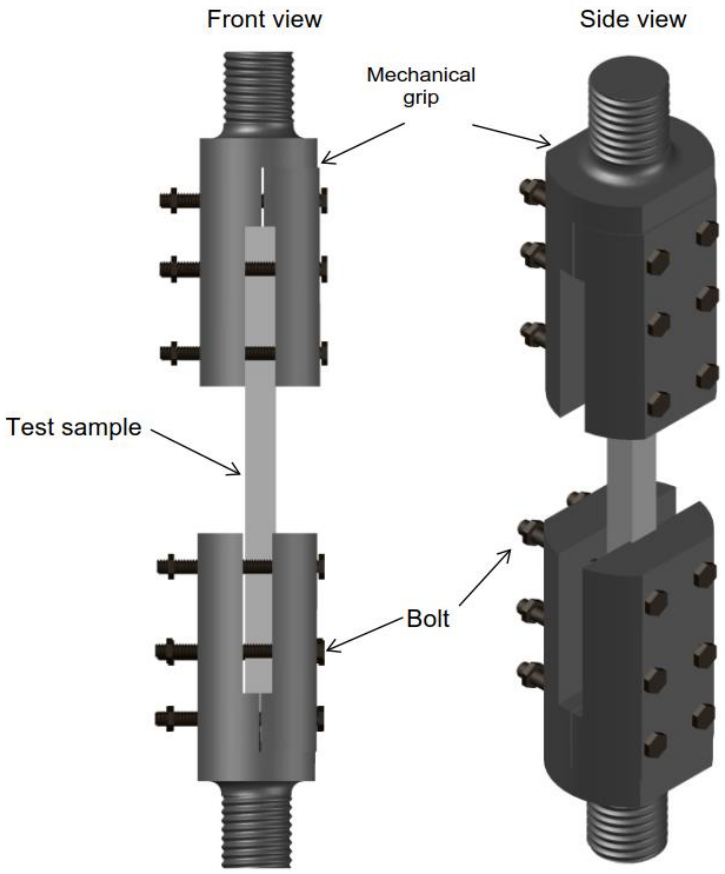

Figure 4.3: 3D model of mechanical grips holding the test sample.

4.2.3 Magnetic circuit design

In order to magnetize the test sample, two sets of coils and a U-shape iron core have been designed as shown in Figure 4.4. The idea was to magnetize the test sample till it reaches its saturation level. Ampere's law in (4.8) was utilized to calculate the magnetic field intensity for the test sample [59]. The constant value of the magnetic flux density was chosen B = 1.57 T for which the value of magnetic field intensity inside the steel bar and U-core was obtained from the *B-H* curves plotted using the data given by the manufacturer as shown in Figure 4.5. The material utilized for making U-core was silicon iron whereas the test sample was made up of structural steel. The permeability of silicon iron is high as compared to steel, therefore, the magnetic field inside the steel bar, air gap and the U-core was calculated separately. The values of H_{bar} and H_{core} were obtained from the plots of the magnetization curves of the material whereas the value of H_{air} was calculated using $B = \mu_o H_{air}$, where μ_o refers to permeability of the free space taken as $4\pi x10^{-7}$ H/m.

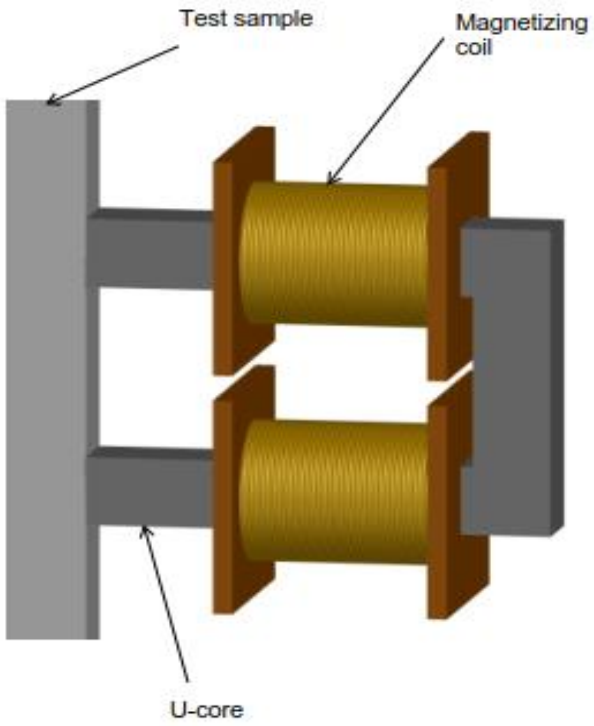

Figure 4.4: *3D model of the magnetizing coil and U-core.*

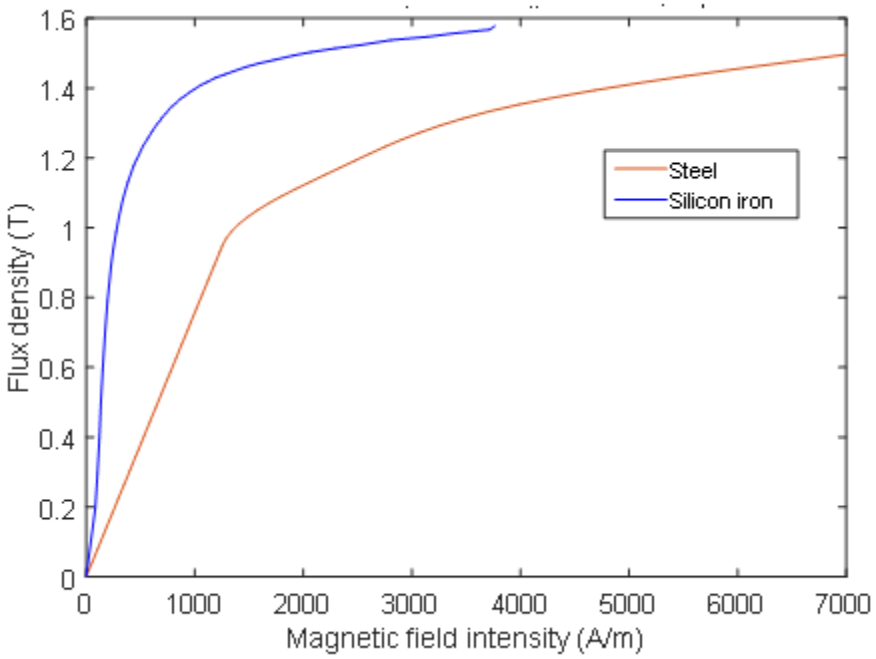

Figure 4.5: *B-H curves for steel bar and core.*

Ampere's law in (4.8) is given as

$$NI = H_{\text{bar}}L_{\text{bar}} + H_{\text{core}}L_{\text{core}} + H_{\text{air}}L_{\text{air}} \tag{4.8}$$

where N is the number of turns, I is magnetizing current, H_{bar}, H_{core} and H_{air} represent magnetic field intensity inside the test sample, U-core and air gap respectively whereas

$L_{bar,}$ L_{core} and L_{air} are the respective lengths of the test sample, U-core and the air gap. The total length of the magnetic circuit was chosen based on the calculations done for buckling load and the mechanical design to determine the dimensions of the coil and the total number of turns of the magnetizing coil. The saturation value of B was taken as 1.57 T for which the magnetic field intensity for H_{bar} and H_{core} was interpolated from the manufacturer data from the Figure 4.5 to be 9944 A/m and 3010 A/m and the overall length of the magnetic circuit was taken as 380 mm. Once the magnetic field intensity and total length of magnetic circuit were known, the number of turns for the coil were then calculated to be N = 628 for the magnetizing current of 5 A. After that the current density (4.9) and wire diameter (4.10) were calculated as

$$J = I / A, \tag{4.9}$$

$$D = 2\sqrt{A/\pi}, \tag{4.10}$$

where I is current, A is the wire's area, J represents the current density and D is the wire diameter respectively. The diameter of the wire was calculated using (4.10) for the specified magnetizing current and the calculated current density was 5.88 A using (4.9) for the wire thickness of 1 mm^2. The actual wire diameter of 1.02 mm including insulation was then utilized for the magnetizing coil. The bobbin (coil former) was designed based on the calculated parameters of the magnetizing coil. In order to avoid excessive heating of the coil, the numbers of layers were chosen carefully during the design process. The number of layers in winding were chosen to be less than 10 for which the inner length of the bobbin was taken as 50 mm initially. Based on the selected dimensions turns per layer and number of layers were computed as

$$T_{layer} = \frac{L_{bobbin}}{D}, \tag{4.11}$$

$$W_{layer} = \frac{N}{T_{winding}}, \tag{4.12}$$

where T_{layer} are number of turns per layer, L_{bobbin} is the length of the bobbin, D is the wire diameter and N are the number of turns. The fill factor was also taken into account during the design process of bobbin in order to accurately calculate the area occupied by the winding. The fill factor is defined as the actual area which can be filled by the winding. The fill factor was taken as 0.7 which means that 70% of the area can be occupied by the winding.

The final dimensions for the bobbin were calculated to be 50 mm x 16 mm with 48 turns per layer and 6.7 winding layers. Based on the calculations, the two sets of bobbins were designed as shown in Figure 4.6.

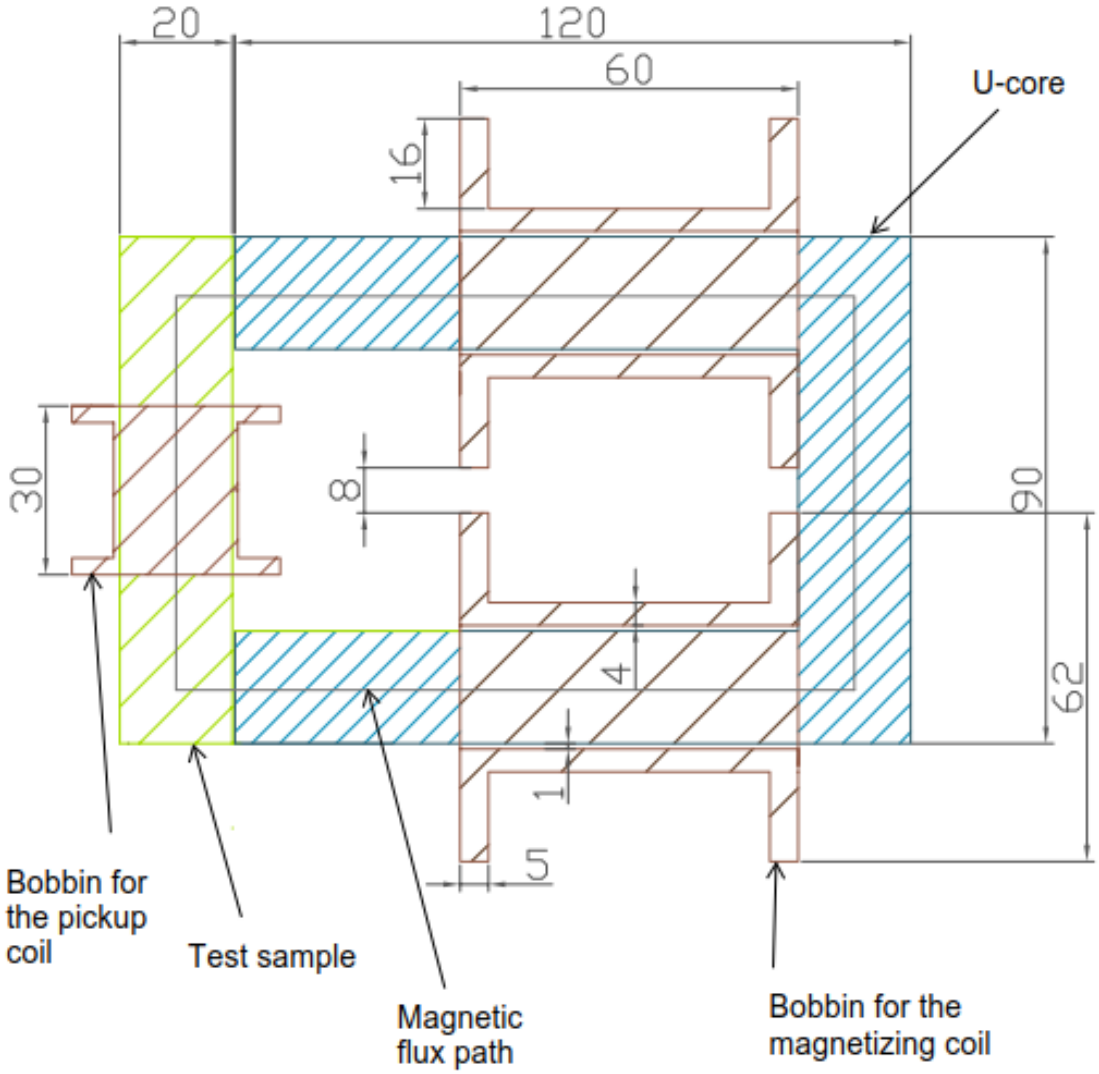

Figure 4.6: *schematic diagram for magnetic circuit.*

The design parameters for the pickup coil were governed by the free space left between the U-core and the mechanical grip as seen from Figure 4.7a. The total number of turns for the pickup coil are 200 using 0.5 mm thick copper wire. The 2D schematic diagram of the magnetic circuit is given in Figure 4.6 which show the overall dimension of the magnetic circuit.

4.3 Working principle of the device

The working principle of the energy harvester is explained in Figure 4.7a and magnetic circuit of the energy harvester is shown in Figure 4.7b. The steel bar was inserted inside the mechanical grips which were then attached to the hydraulic press machine for the application of mechanical stress from axial direction as explained in Figure 4.7b. The test sample was first magnetized using AC magnetization and stressed statically for different

tensile and compressive stress values in order to determine the magnetization curves. After determining the magnetization curves, the test sample was then magnetized using DC magnetization and stressed dynamically inducing voltage in the pickup coil. The induced voltage in the pickup coil is due to Villari effect explained in Chapter 2.

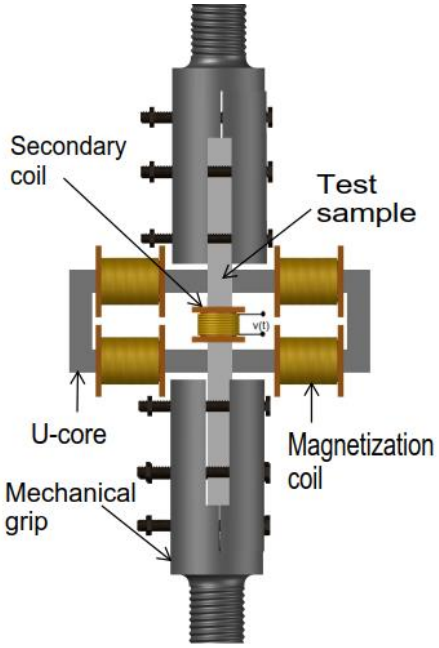

Figure 4.7a: *Working principle of the energy harvesting device.*

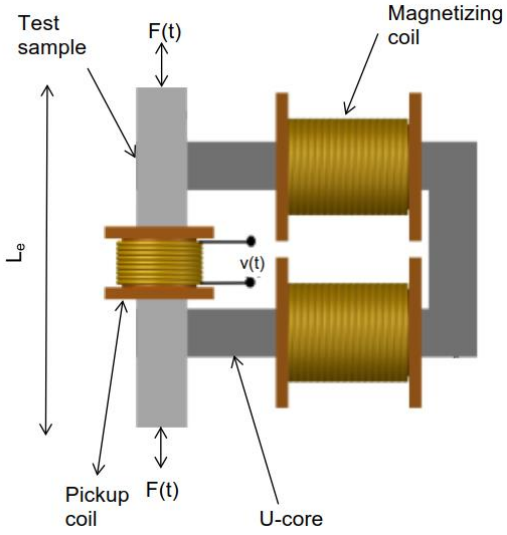

Figure 4.7b: *Magnetic circuit for energy harvester.*

The experimental setup for measuring the *B-H* curves for the test sample is explained using block diagram in Figure 4.8.

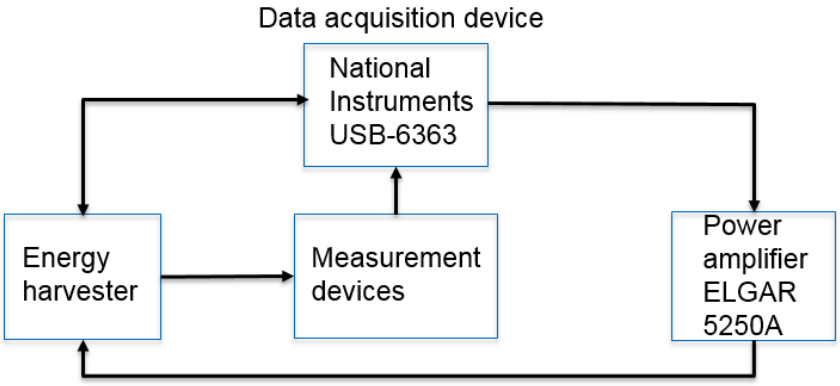

Figure 4.8: *Block diagram explaining the steps involved to measure magnetization curves.*

National Instruments data acquisition device was used to provide an interface between measurement devices (current probe and differential probe) and the energy harvester. The data acquisition device gets the data from measurement devices and calculates the output based on the measurement method developed in Chapter 5. The output signal from National Instruments cannot drive the magnetic circuit because of low power signal, thus the

output first goes to a power amplifier (ELGAR 5250A) for amplification. The amplified signal was then supplied to the magnetizing coil. The test sample was stressed statically afterwards to measure the magnetizing curves under different stress values.

The output voltage and power were measured while applying cyclic loading under DC magnetization and the maximum power was calculated using variable load resistor through impedance matching. The actual laboratory setup is given in Figure 4.9.

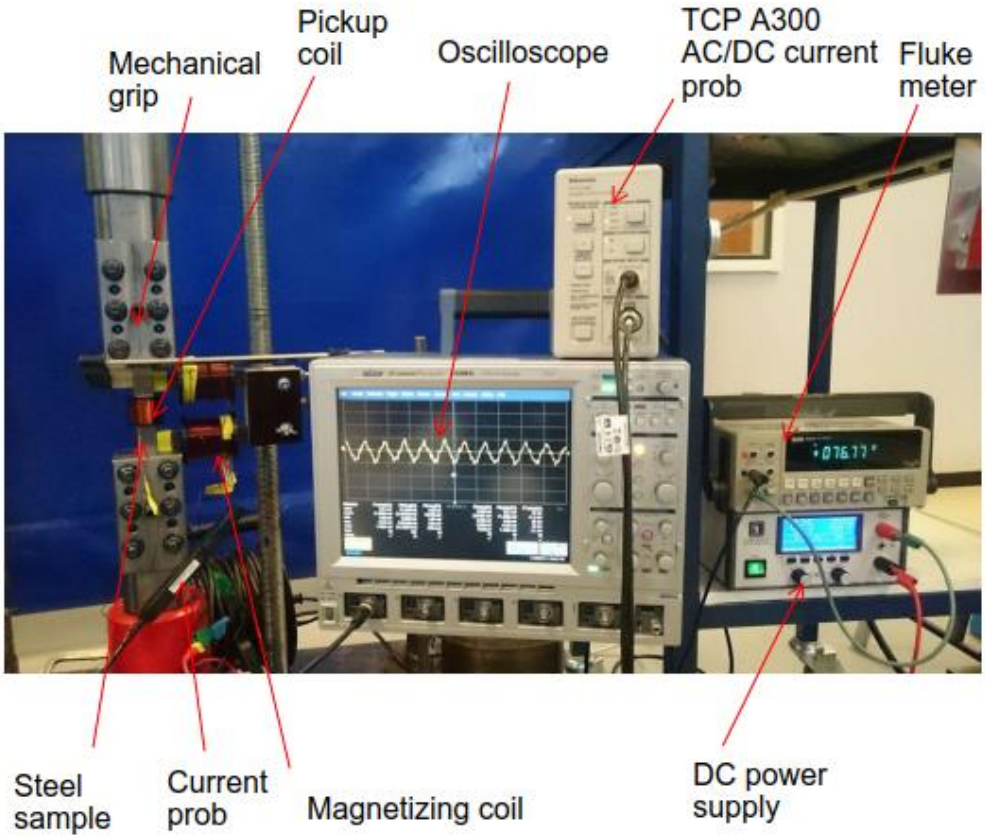

Figure 4.9: *Experimental setup of the energy harvester.*

5. PROPOSED METHOD FOR MAGNETIZATION CURVES

This chapter explains the experimental methods utilized to determine the magnetization curve for the test sample under static stress. The proposed method utilizes the data (magnetizing current and flux density) obtained from the measurement method developed in [5] and [60]. According to [60], to obtain the sinusoidal flux density *B* in the test sample, a feedback control system must be designed in order to control the waveform shape of the pickup coil voltage. The feedback control system can either be designed using analog electronic circuits such as operational amplifiers and filters etc. or it can be designed digitally using computer software. The feedback system based on analog circuits causes distortion in the generated output signal for higher values of flux density due to oscillation in the amplitude of the control signal as discussed in [60]. The advantage of using digitally designed feedback control system involves designing distortion free low pass filters, oscillation free feedback loop and offers great controllability over the controller gain for achieving controlled excitation while carrying out magnetic measurements. However, because of the non-linear behaviour of the magnetic circuits, the final output cannot be obtained by single iteration, thus, the digital feedback system design takes more time to compute the final waveform because of the number of iterations involved [5]. The block diagram explaining the steps involved in obtaining the magnetization curve is given in Figure 5.1.

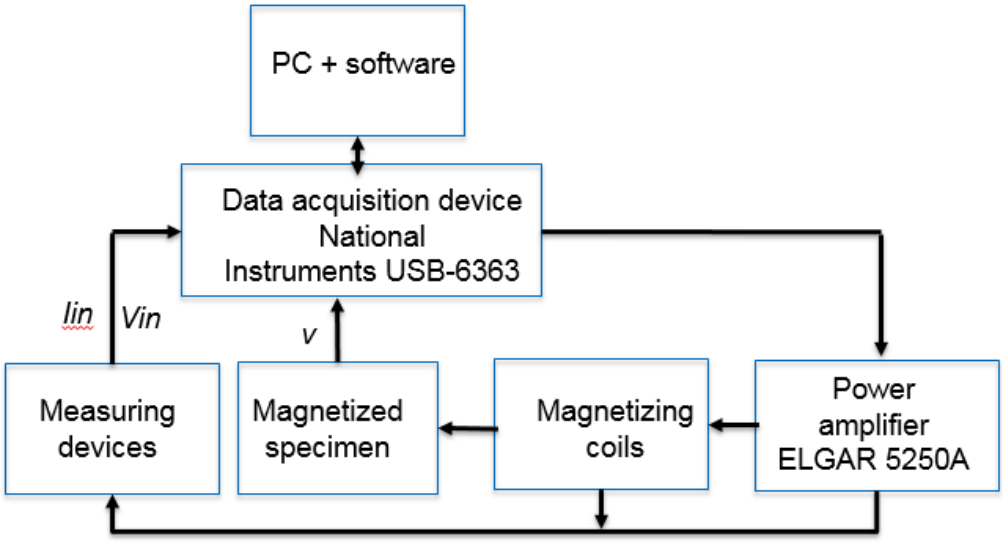

Figure 5.1: *Block diagram of the experimental setup for measuring magnetization curves.*

5.1 Measurement method and control algorithm

As discussed earlier, non-linear nature of the magnetic circuit demands designing a waveform control system in order to obtain sinusoidal flux density *B* inside the test sample. To do so, the control method of the waveform developed in [5] was first utilized for measuring the magnetizing current and the corresponding sinusoidal magnetic flux density. The algorithm was implemented using MATLAB where the input parameters of the magnetic circuit, frequency of the excitation voltage and the desired flux density were given in the start. The required output voltage $v_c^{(i+1)}$ (5.1) from the data acquisition device was calculated to obtain the desired sinusoidal magnetic flux density inside the test sample given as

$$v_c^{(i+1)} = v_c^{(i)} - K\frac{V_{C1}^{(i)}}{V_{B1}^{(i)}}(v_B^{(i)} - v_{Br}), \tag{5.1}$$

where i represents the number of iterations, $v_c^{(i)}$ is the output voltage generated by data acquisition device NI USB-6363 as shown in block diagram, v_B is the measured voltage from the pickup coil, K is the gain of the control system, $V_{C1}^{(i)}$ and $V_{B1}^{(i)}$ are the fundamental harmonic components of the generated voltage $v_c^{(i)}$ and the pickup coil voltage $v_B^{(i)}$, respectively computed using Fourier transform and v_{Br} is the measured voltage corresponding to the desired sinusoidal flux density *B*. To start the iteration, the initial voltage v_c generated by DAQ device was first taken to have smaller amplitude. The voltage is then multiplied by gain during the amplitude control and waveform control method to obtain desired sinusoidal flux density. The signal generated by the data acquisition device cannot be fed directly to magnetizing coil because the device can supply maximum ±7.5 V with the maximum current of 500 mA. Therefore, the signal was first amplified using a power amplifier (ELGAR 5250A) and then supplied to the magnetizing coil as explained in Figure 5.1. The same steps were repeated for the excitation voltage v_c until sinusoidal flux density was obtained inside the test sample.

The measured output voltage from the pickup coil was then integrated to obtain the magnetic flux density given in (5.2) as

$$B(t) = \int \frac{v(t)}{NA} dt, \tag{5.2}$$

where $v(t)$ is the voltage from the pickup coil, N is the total number of turns in the pickup coil and A is the area of the test sample.

5.2 Proposed method

The measurement method developed in [5], [60] and [61] utilizes single sheet test sample to measure the value of B and corresponding value of H using H coil placed near the test sample in [5] or wound around the paramagnetic former in [61]. Whereas the test sample in the proposed energy harvesting device consists of steel sheets joined in the form of a stack as discussed in Chapter 4. The TMR (tunnelling magneto resistive) sensor was first tested to measure magnetic field on the surface of the test sample but the measured results were not accurate because determining the suitable place for attaching the sensor over the test sample was difficult. Therefore, a new method was proposed based on Ampere's law to compute the magnetic field for the steel sample. The measurement method discussed in [5] and [60] was first utilized to compute sinusoidal values of magnetizing current I and the flux density B when the test sample was magnetized under AC magnetization and static stress. Integration of Ampere's law (5.3) around the flux path gives

$$NI(B,\sigma) = H_{\text{bar}}(B,\sigma)L_{\text{bar}} + H_{\text{core}}(B)L_{\text{core}}, \tag{5.3}$$

where B is the magnetic flux density, σ is the stress, I refers to magnetization current which depends on B and σ, N is the number of turns in the magnetization coils. H_{bar} and H_{core} are the magnetic field strength in the test sample and u-core, respectively, whereas L_{bar} and L_{core} are the corresponding magnetic circuit lengths. The flux density has been calculated by integrating the secondary voltage using (5.2), and the excitation voltage has been iterated so as to obtain a sinusoidal flux density into the test sample as discussed in [60].

Two different methods were tested to obtain B-H curves for the test sample. The first method is based on plotting single-valued $I(B, \sigma)$ curves by tracing the tips of hysteresis loops obtained for different flux density amplitudes as shown in Figure 5.2.

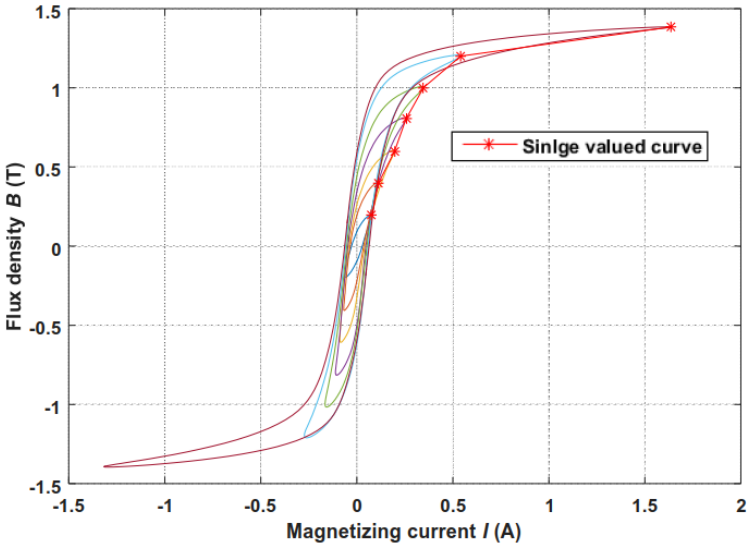

Figure 5.2: *Single valued B-I curve plotted against tips of the hysteresis loops.*

The $H_{\text{core}}(B)$ curves were known from previous measurements and thus the magnetization curves for the test sample were obtained as

$$H_{\text{bar}}(B,\sigma) = \frac{NI(B,\sigma) - H_{\text{core}}(B)L_{\text{core}}}{L_{\text{bar}}}, \tag{5.4}$$

The second method for obtaining the *B*-*H* curve involves taking the *B*-*I* curve hysteresis loop when the material reaches its saturation and obtaining the sinusoidal value of *B* as discussed earlier. The magnetic field inside the test sample was calculated using (5.4). The weighted average curve was then calculated such that it gradually approaches to the ascending branch when *B* approaches to positive saturation and approaches descending branch when *B* approaches to negative saturation receptively. The hysteresis loop along with the weighted average curve is shown in Figure 5.3.

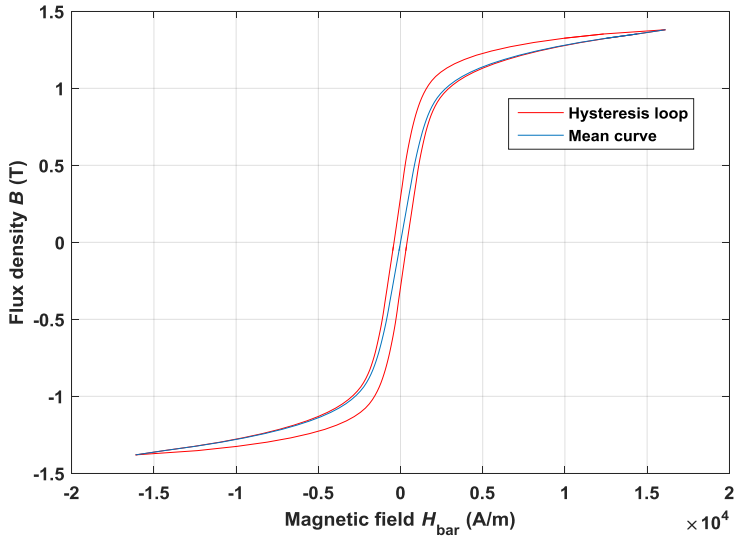

Figure 5.3: *Hysteresis loop and weighted averaged B-H curve of the test sample.*

6. RESULTS

This chapter discusses the results obtained from the measurement method to obtain the magnetization curves and the experimentation in order to validate the proposed method by comparing the theoretical and experimental results. The method developed in Chapter 5 was utilized to determine the magnetization curves (*B-H* curves) for the test sample. There is no unique solution available which can accurately evaluate the magnetization curves, thus two different methods were tried to compare the results of the measurement method with the experimental results of the tested methods.

A hydraulic press machine was utilized for the application of mechanical stress as discussed in Chapter 4. In order to understand the behaviour of magnetization curves under mechanical stress, different tensile and compressive stress values were chosen keeping in view that the applied load does not exceeds the buckling load. Three different test samples were constructed for the experimentation for which the dimensions are given in Chapter 4. Two of the samples were constructed using 1 mm and 1.5 mm thick steel sheets and the third sample was constructed using solid steel bar. The buckling load was measured to verify the calculations made in Chapter 4. The maximum tensile and compressive stress that can be applied to the test sample were recorded 100 MPa and -25 MPa for the stack of 1 mm thick steel sheet, 100 MPa and -30 MPa for the stack of 1.5 mm thick steel sheet whereas 100 MPa and -100 MPa for solid steel bar. It was concluded from the stress tests that the calculation for buckling load applies only to the solid structures and it is not applicable for sample made up of steel sheets joined together in the form of stack. Thus, the experimentations were carried out using static tensile stress values of 25 MPa, 50 MPa, 75 MPa and 100 MPa and the compressive stress values of 5 MPa, 10 MPa, 15 MPa and 20 MPa respectively, for all samples.

6.1 Static stress tests for *B-H* curves

In order to determine the magnetization curves, the test sample was first stressed statically under AC magnetic biasing for selected compressive and tensile stress values. The experimental setup explained in Chapter 5 was utilized to obtain the magnetization curves (*B-H* curves) where the excitation voltage was supplied using a power amplifier at frequency of 10 Hz.

Two different methods were tested to compute the *B-H* curves under different tensile and compressive static stress values and the results were compared to determine the suitable method as discussed in Chapter 5.

- **Method 1**

The first method involved obtaining a single valued magnetization curve in which the value of *B* was selected at maximum value of the magnetizing current after iterating the excitation voltage to obtain the sinusoidal value of the flux density. After computing $I(\sigma, B)$, the magnetic field inside the test sample was calculated using Ampere's law (5.6). The *B-I* hysteresis loop and the single valued curve obtained by tracking the tips of the hysteresis loop is shown in Figure 6.1 and Figure 6.2.

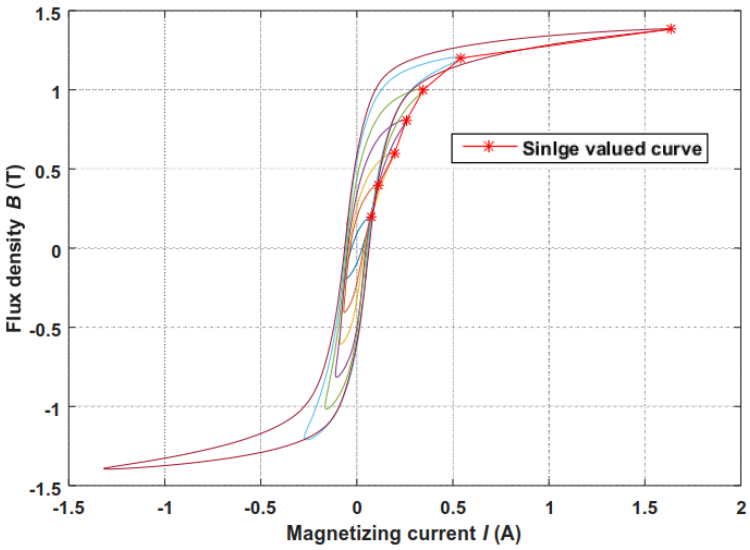

Figure 6.1: *Hysteresis loop and single valued B-I curve.*

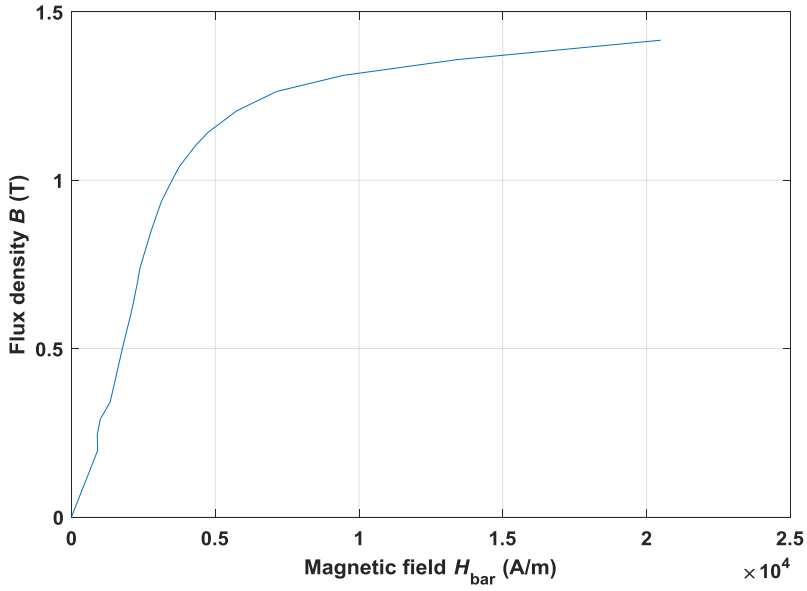

Figure 6.2: *Single valued B-H curve for the stack of steel sheets.*

The test sample was then stressed statically to analyse the behaviour of the magnetization curve under mechanical stress. The results for the single valued *B-H* curves using different tensile stress values are given in Figure 6.3.

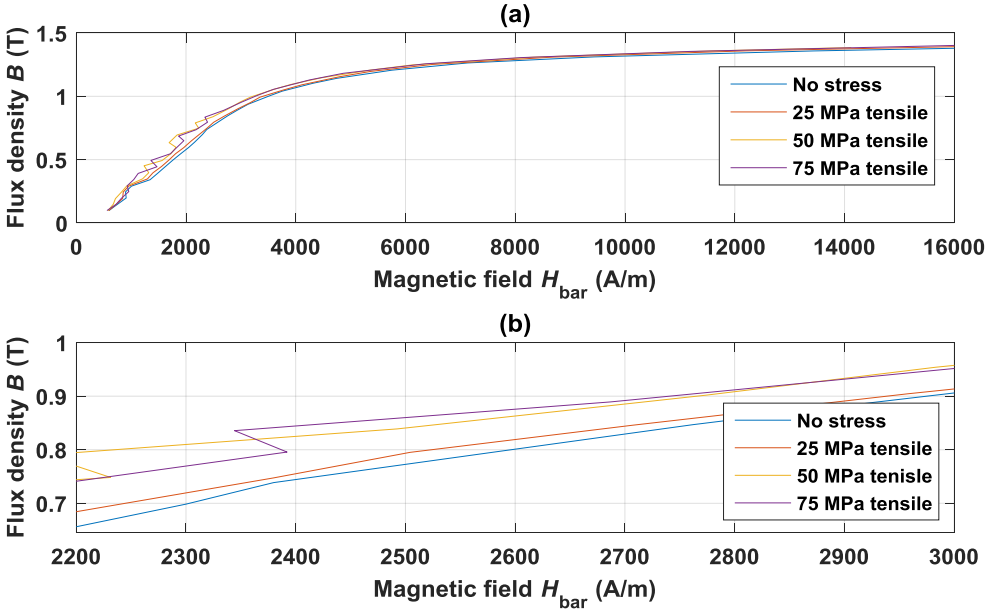

Figure 6.3: *B-H* curves under different tensile stress values (a) and the scaled plot (b) showing the effect of mechanical stress.

The figure shows that the calculated *B-H* curves for different tensile stress values are quite distorted and do not increase monotonically. Also, the distortion is quite prominent for the lower values of magnetic field (H_{bar} < 2400 A/m).

As discussed in Chapter 4, the induced voltage in the pickup coil is due to the rate of change of magnetic flux density (ΔB) under cyclic loading of the test material. In order to determine maximum ΔB value using method 1, difference between the calculated *B-H* curves under stress was calculated. The single valued *B-H* curves plotted for zero and 20 MPa compressive stress are shown in Figure 6.4a and the corresponding value of ΔB obtained by calculating the difference between the two curves is shown in Figure 6.4b.

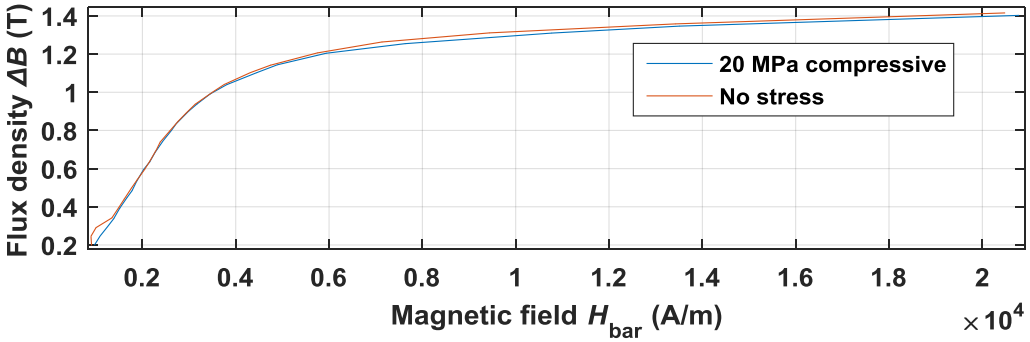

Figure 6.4a: *B-H curves for zero and 20 MPa compressive stress.*

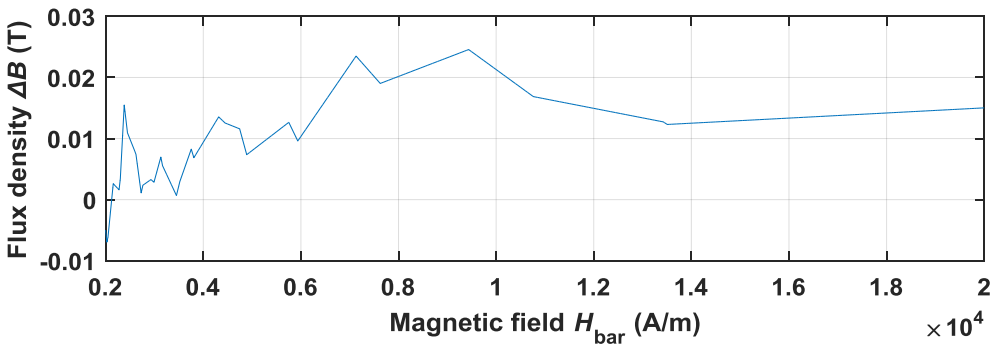

Figure 6.4b: *ΔB for zero to 20 MPa compressive stress.*

The plot for Δ*B* curve in Figure 6.4b shows a lot of variation because the *B*-*H* curves in Figure 6.4a are not increasing monotonically and therefore the difference between the curves is changing inconsistently. The plotted results show that the magnetization curves obtained by tracking the tips of the hysteresis loops were not smooth as the curves were plotted against the discrete data points as shown in Figure 6.3, thus, the method was unable to correctly determine the value of Δ*B*.

- **Method 2**

The second technique for obtaining *B*-*H* curve involves taking the hysteresis loop of magnetization curve when material reaches saturation and then calculating the weighted average curve as discussed in Chapter 5. The weighted average curve was calculated such that it gradually approaches to the ascending and descending branch of hysteresis loop when *B* approaches to positive and negative saturation, receptively. The hysteresis loop along with the weighted average curve is shown in Figure 6.5.

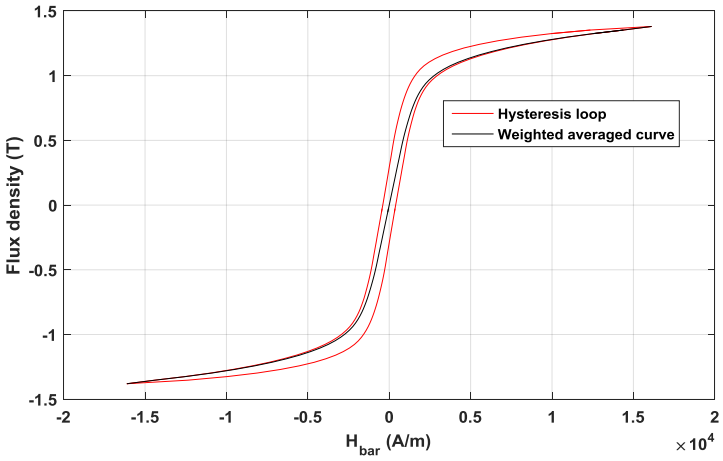

Figure 6.5: *Hysteresis loop and weighted average curve without mechanical stress.*

The experimental data was then plotted using the above mentioned technique to obtain the *B*-*H* curves under static stress. The magnetization curves under different tensile stress

values along with the scaled plot are given in Figure 6.6 whereas the magnetization curves for different values of compressive stress and the scaled plot are given in Figure 6.7.

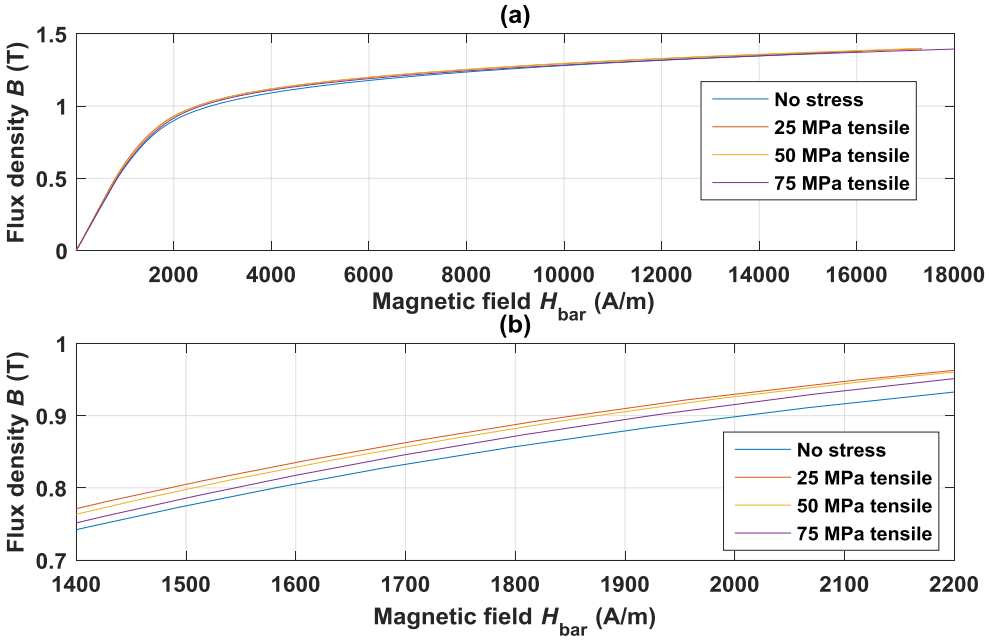

Figure 6.6: *Weighted averaged B-H curves (a) and the scaled plot (b) under different tensile stress values.*

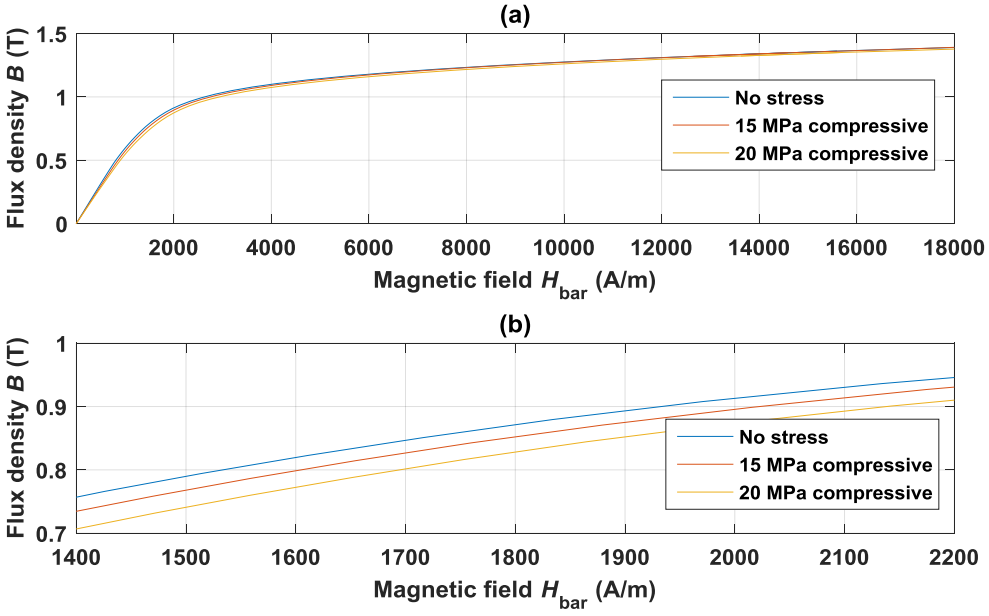

Figure 6.7: *Weighted averaged B-H curves (a) and the scaled plot (b) under compressive stress.*

By examining Figure 6.6 (b) it can be seen that the permeability of the material increases due to the application of tensile stress up till a certain point after which it again starts

decreasing. The tensile stress value from zero to 25 MPa causes increase in the permeability of the material whereas for 50 MPa it again starts decreasing. By analysing Figure 6.7 (b), it can be seen that the permeability of the material decreases when the compressive stress was applied to the test sample.

After obtaining the weighted averaged *B*-*H* curves from the hysteresis loop, the values of Δ*B* were computed by calculating the difference among the *B*-*H* curves plotted for different stress values. Figure 6.8 (a) and Figure 6.9 (a) show the plots for the magnetization curves for zero and 25 MPa and zero and -20 MPa static stress whereas the corresponding Δ*B* curve is given in Figure 6.8 (b) and Figure 6.9 (b).

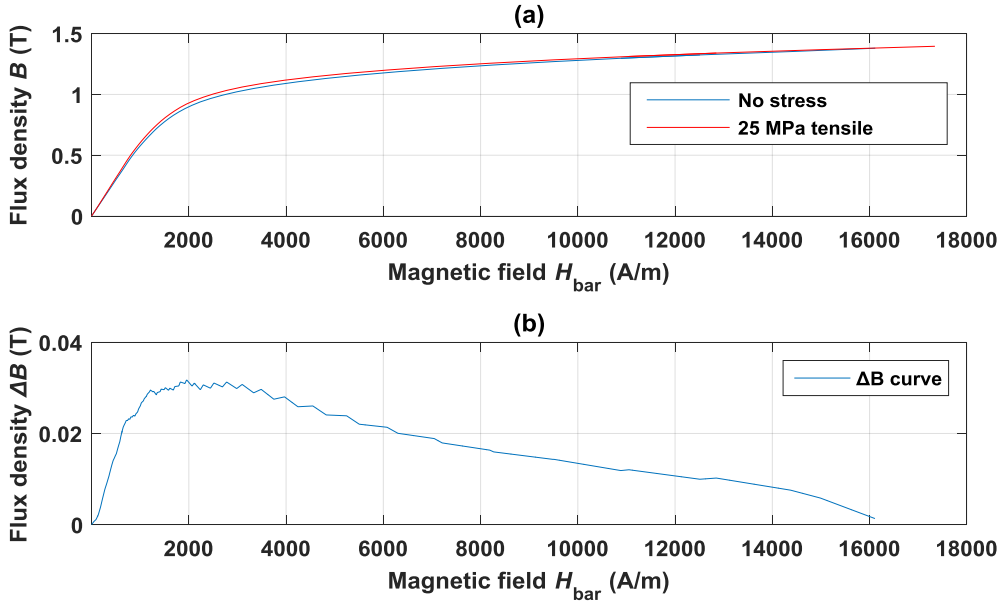

Figure 6.8: *The weighted averaged B-H curves (a) and the ΔB curve (b) for 0 and 25 MPa tensile stress.*

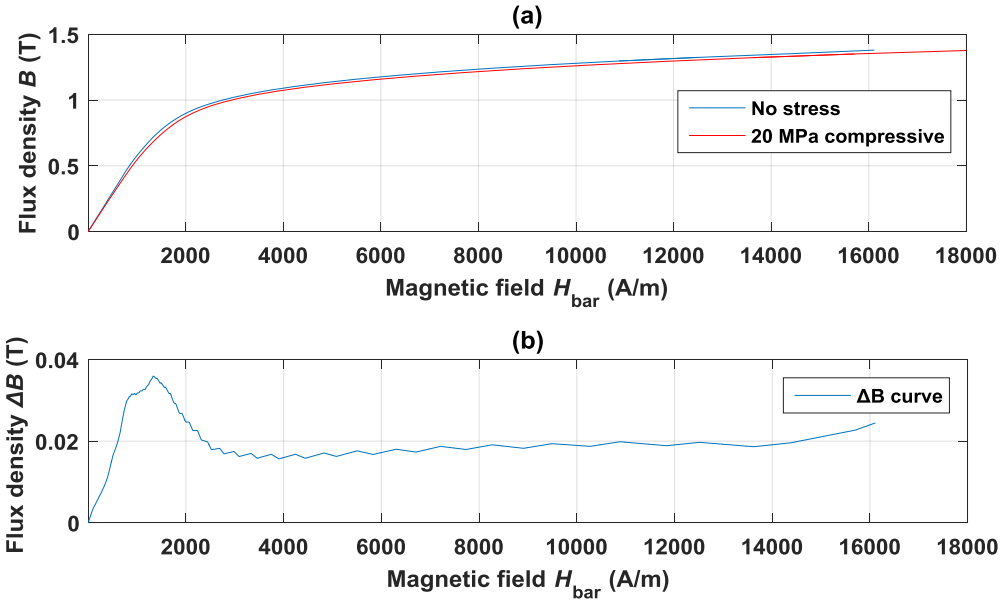

Figure 6.9: *The weighted averaged B-H curves (a) and the ΔB curve (b) for 0 and 20 MPa compressive stress.*

As seen from the above figures, the *B-H* curves and the *ΔB* curve obtained by using method 2 appears to be more consistent where the increasing and decreasing trend can be seen clearly from the *ΔB* curve. Thus the weighted averaged curve of the hysteresis loop was utilized to determine the maximum value of *ΔB* under different stress values.

6.2 Cyclic loading test

In order to validate the proposed method, the test sample was magnetized using DC magnetization and then cyclic loading was applied inducing voltage in the pickup coil as discussed in Chapter 5. The experiments were carried out using different values of cyclic stress at different frequencies in order to determine the effect of the amplitude and frequency of the mechanical vibrations upon induced voltage. The experimental values for the amplitude and frequencies of the cyclic stress are given in Table 6.1.

Table 6.1: *The experimental values of cyclic stress.*

Experiment	Peak to peak variation of the cyclic stress (MPa)	Peak-to-peak value of the cyclic stress (MPa)	Frequency of the cyclic stress (Hz)
1	2.5 – 25	22.5	11
2	0 – -15	15	11
3	0 – -20	20	11
4	-15 – 15	30	11
5	10 – -13.5	23.5	11
6	2.5 – 25	22.5	8
7	2.5 – 12.5	10	20

Experiments were performed using both solid sample and the sample made by steel sheets. The peak to peak and root mean square (RMS) values of the pickup coil voltage were measured using oscilloscope for the above mentioned experimental cases. The output signal was digitally filtered to filter out 50 Hz noise signal and high frequency noise signal coming from ground wire and the electrical apparatus nearby. It was observed that the induced voltage increases by increasing the frequency of vibrations and the maximum amplitude of the pickup coil voltage for experiment 7 was recorded 21.7 mV (Vrms) when the peak-to-peak value of the vibration was only 10 MPa. Whereas for experiment 6 the maximum amplitude of the pickup coil voltage was measured 14.8 mV (Vrms) when the peak-to-peak value of the cyclic stress was 22.5 MPa.

The induced voltage in the pickup coil is due to the movement of domain walls of the construction steel material upon external magnetization. As the magnetic field is increased, the magnetostriction in the magnetizing direction first increases and then shows a maximum when the rotation of the domain magnetization starts to occur. Since the stress affects the domain structure through magnetoelastic interaction, the maximum magnetostriction shows the stress dependence [62]. The induced voltage must decrease when material reaches saturation as discussed in Chapter 2. To verify this, the experiments were carried out first using test sample made up of steel sheets. The experimental results for the induced voltage (Vrms) upon DC magnetization under different peak-to-peak values of cyclic loading are given in Figure 6.10.

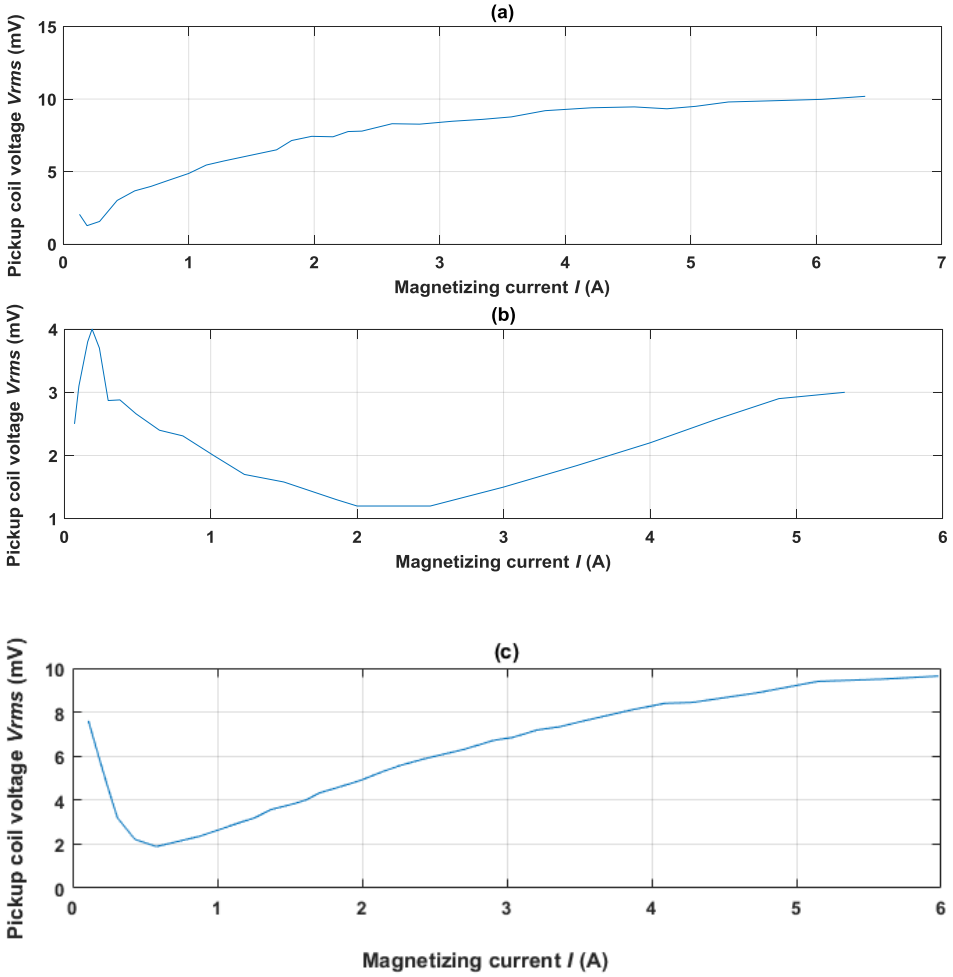

Figure 6.10: *Pickup coil voltage and magnetizing current for (a) 2.5 MPa to 25MPa, (b) zero to -20 MPa and (c) 15 MPa to -15 MPa using stack of steel sheets sample.*

The results from the figure show that the induced voltage first decreases but then it again starts increasing when the DC magnetizing current increases from zero to 6 A. The continuous increase in the induced voltage shows that the material was not going to saturation by increasing the applied magnetic field. It was observed that while applying cyclic loading, the air gap between the plates of the sample was changing because the sheets were joined only by welding from both ends. The free length of the test sample was not clamped or glued to hold the steel sheets together. Thus, slight buckling in the sheets was causing continuous change in the air gap as well as the length of the magnetic circuit and because of that the material was not able to go into saturation even though the magnetic field was increasing. The rise in the induced voltage may be due to the fact that there was back EMF (electromotive force) generated by the relative movement of individual sheets.

Similar experiments were then performed using a solid test sample having exact same dimensions and the induced voltage from the pickup coil was then measured under cyclic loading as shown in Figure 6.11.

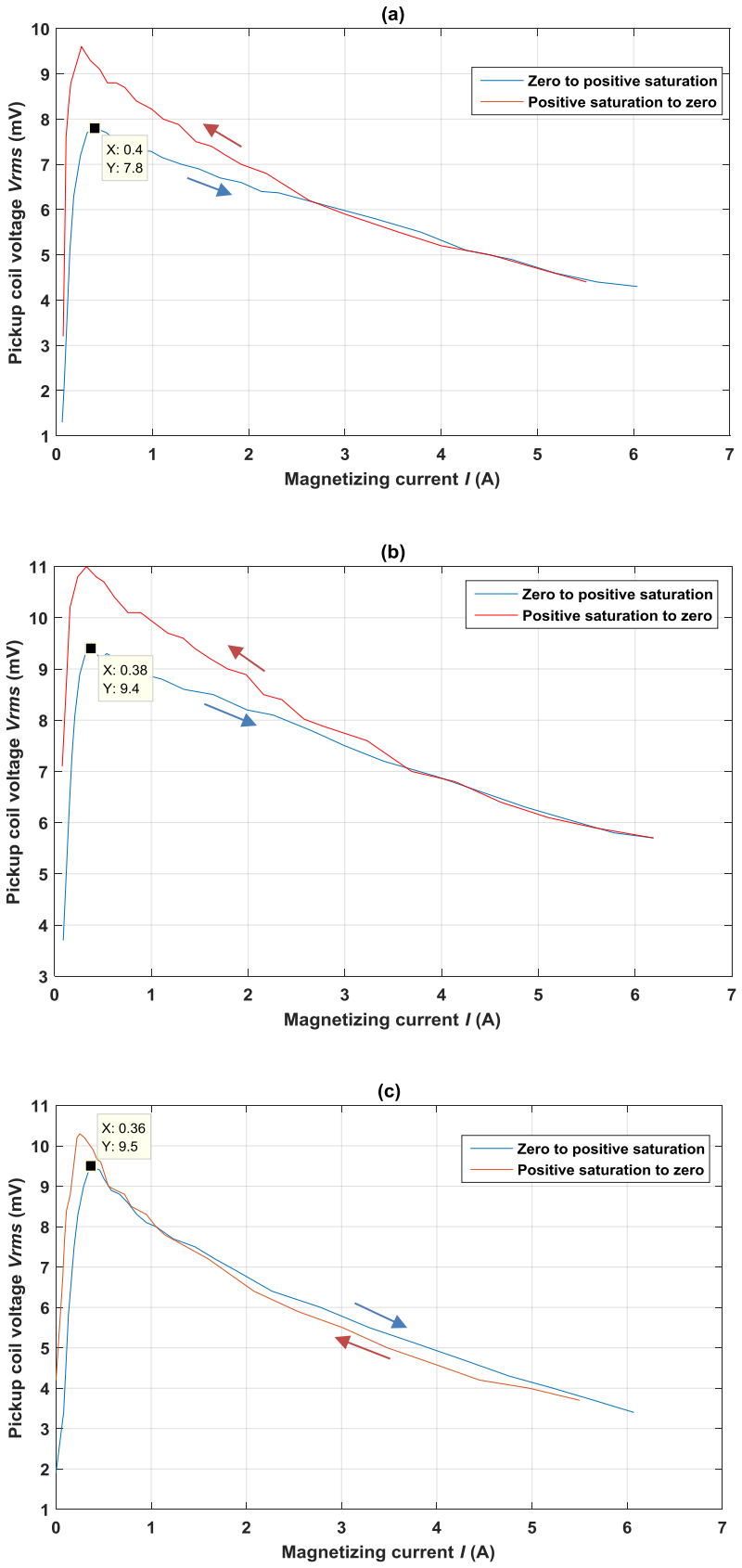

Figure 6.11: *Plot for induced voltage and magnetizing current for (a) 2.5 MPa to 25MPa, (b) 15 MPa to -15 MPa and (c) 0 MPa to -20 MPa using solid test sample.*

Figure 6.11 shows the hysteresis curve plotted by varying the magnetizing current from zero to 6 A and then again back to zero and measuring induced voltage (Vrms) in the pickup coil at various intervals under different cyclic loading. It was observed that the magnetic flux was not zero even when there was no applied magnetic field which refers to as residual magnetic flux. By increasing the magnetizing current, the magnetic field increases slowly till material reaches positive saturation. The induced voltage first increases in the start and reaches maximum where the ΔB is maximum and then starts decreasing as material reaches its saturation shown by the blue curve in Figure 6.11. After that, the magnetizing current was decreased slowly to track the hysteresis curve as material returns from positive saturation to zero shown by the red curve. It was observed that the induced voltage at $I = 0$ was higher for red curve as compared to blue curve. This is because of remanence defined as the ability of the material to retain a certain amount of residual magnetism when the magnetizing field is removed after achieving saturation.

The amplitude of the induced voltage should be maximum when ΔB is maximum. To verify that, the magnetizing current (I) was calculated at maximum value of ΔB taken from Figure 6.8 and 6.9. The results after calculations show that for zero to -20 MPa static stress the maximum value of ΔB from the Figure 6.11 (b) was 0.037 T for which the magnetizing current was computed as $I = 0.2750$ A. Likewise, the maximum ΔB value for zero to 25 MPa static stress in Figure 6.10 (b) was 0.031 T and the calculated magnetizing current value was $I = 0.3883$ A. The peak-to-peak value of the induced voltage was calculated as

$$V = 2\pi fNA\Delta B, \tag{6.1}$$

where V is the pickup coil voltage, f is the frequency of the cyclic loading, N are number of turns in the pickup coil, A is the area of the test sample and B is the magnetic flux density. The peak-to-peak value of the induced voltage calculated for $\Delta B = 0.037$ T was 81.8 mV and for $\Delta B = 0.031$ was 68.86 mV respectively. During cyclic loading, the frequency of mechanical vibration was 11 Hz, the cross section area of the test sample was 400 mm^2 and number of turns in the pickup coil were 80. It can be seen that the peak amplitude of the induced voltage in Figure 6.11 (a) is 7.8 mV (Vrms) at $I = 0.4$ A for which the peak-to-peak value was computed as 22.01 mV for zero to positive saturation curve. Likewise, the maximum amplitude of the induced voltage in Figure 6.11 (c) is 9.5 mV (Vrms) at $I = 0.38$ A for which the peak-to-peak value was computed as 27 mV for zero to positive saturation curve. The deviation in the calculated and measured results was due to the fact that the eddy current losses or hysteresis were not taken into the account while doing the calculations for the induced voltage.

- **Maximum power point measurement**

In order to compute the average output power, the amplitude of the induced RMS voltage was first selected for maximum ΔB value under given cyclic loading. The output power

was then computed by changing the load resistance and measuring the peak to peak voltage with the help of an oscilloscope. The results for the output power plotted against the load resistance using different cyclic loading values are presented in Figure 6.12.

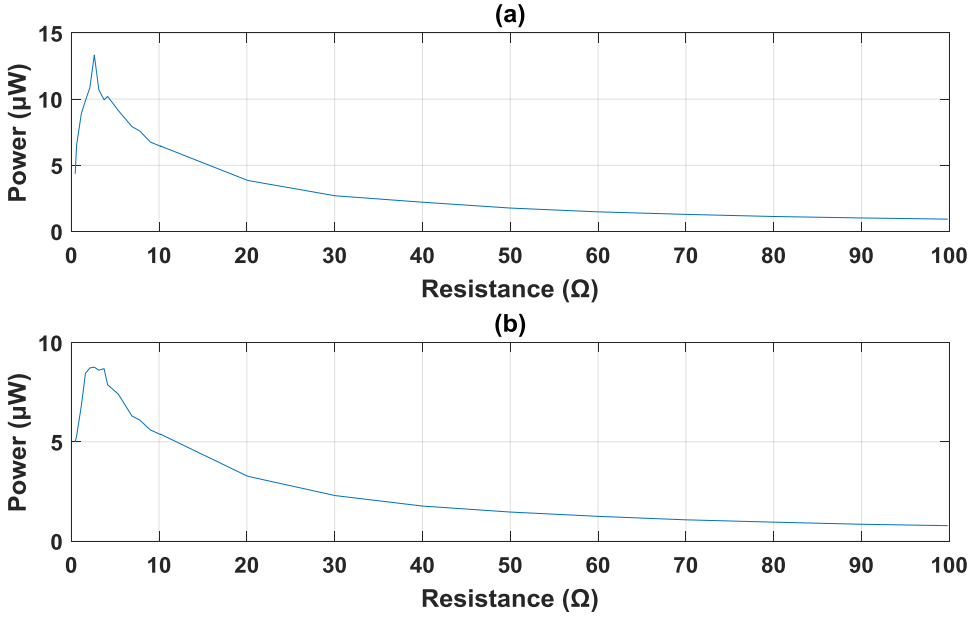

Figure 6.12: *Output power for zero to -20 MPa (a) and 2.5MPa to 25 MPa (b) of cyclic stress values*

The pickup coil used for the solid test sample consists of 80 turns and resistance of the pickup coils was measured 1.65 Ω with the help of the fluke meter. The output power was computed using RMS voltage measured from the pickup coil. Figure 6.12 (a) shows that the maximum power of 13.3 μW can be obtained under the cyclic loading from zero to -25 MPa and the maximum power of 8.76 μW can be obtained under the cyclic loading from 2.5 MPa to 25 MPa using load resistance of 2.62 Ω. Also, the output power calculated by measuring peak-to-peak voltage was recorded as 121 μW and 119 μW for zero to -25 MPa and 2.5 MPa to 25 MPa using load resistance of 2.62 Ω, respectively.

7. DISCUSSION

The discussions regarding the achieved results and the possible sources of errors resulting in deviation from the achieved results are presented in this chapter. The main objective of the thesis was to determine the feasibility of employing construction steel material for vibration based energy harvesting. To do so, the magnetization curves for the test sample were first obtained based on the measurement method developed in [5] and then utilizing the proposed method as discussed in Chapter 5. It was observed that the control algorithm cannot be utilized to measure *B-H* curves if the frequency of the excitation voltage is less than 8 Hz. It was due to the fact that the waveform control method was not possible for lower frequencies due to large distortion and requires a lot of iterations so the specified tolerance level of error never reaches as discussed in [5]. Thus the experiments were performed using excitation frequencies of 10, 15 and 20 Hz for the purpose of comparison. Also, in order to compute the *B-H* curve, the digitally filtered values of the pickup coil voltage and *I* were taken to remove the distortion from the magnetization curve as shown in Figure 7.1

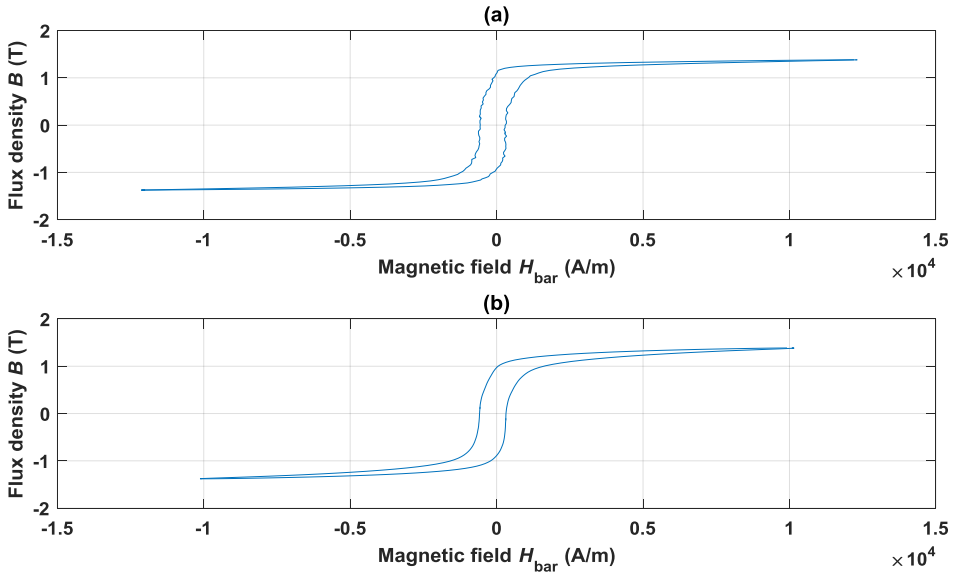

Figure 7.1: *B-H curve before filtration (a) and after filtration (b) of the measured voltage and magnetizing current.*

It was observed that the output signal generated by the data acquisition device also contains the DC component in the waveform which might explain the reason of the shift in the *B-H* curve as shown in Figure 7.2 (a). In order to compute the ΔB values from the plotted *B-H* curves, the shift in the curve was first corrected as shown in Figure 7.2 (b)

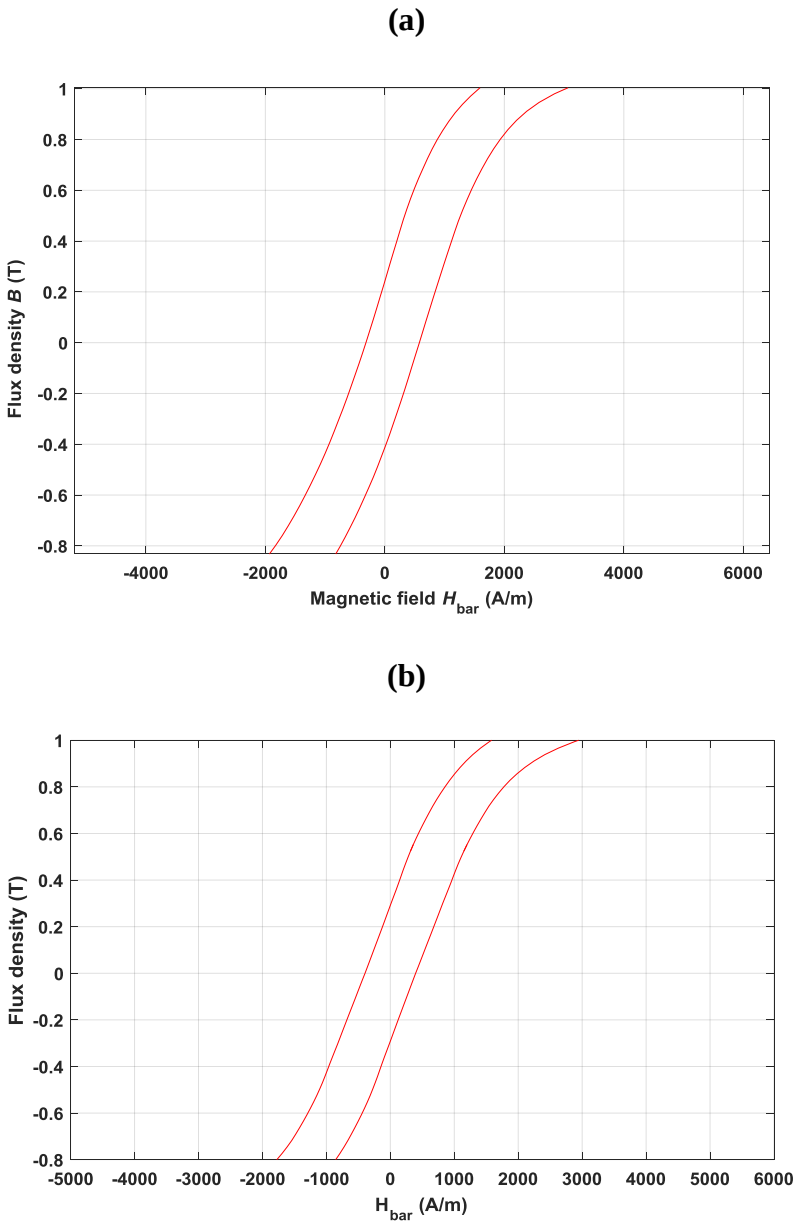

Figure 7.2: *Scaled plot showing shifting of B-H hysteresis loop from the origin (a) and the hysteresis loop cantered in the origin (b).*

In order to measure *B-H* curves under static stress, the buckling load was calculated in Chapter 4. The theoretical value of the calculated buckling load was 99.7 kN for the solid bar and 4.33 kN for single steel sheet. It was observed that the buckling load was quite low for the stack of steel sheets sample (F_{Cr} = 15 kN) as compared to the solid sample because the sheets were only joined by welding at both ends. There was no support in the middle part of the stack, thus the outer sheets were prone to bend quite easily as the load was not evenly distributed throughout the cross-sectional area. Therefore, the buckling load was observed more than the calculated buckling load for the single steel sheet but

much lower than the buckling load computed for solid sample. Also, the calculated buckling load is quite ideal as the classical Johnson's buckling theory does not take into account the eccentric loading conditions.

The U-core was attached to the test sample using steel grips as shown in Figure 7.3. While doing the measurements for the magnetizing curves, the air gap was assumed to be negligible and thus the calculation in the measurement method does not take into the account the magnetic field for the air gap between the core and the sample.

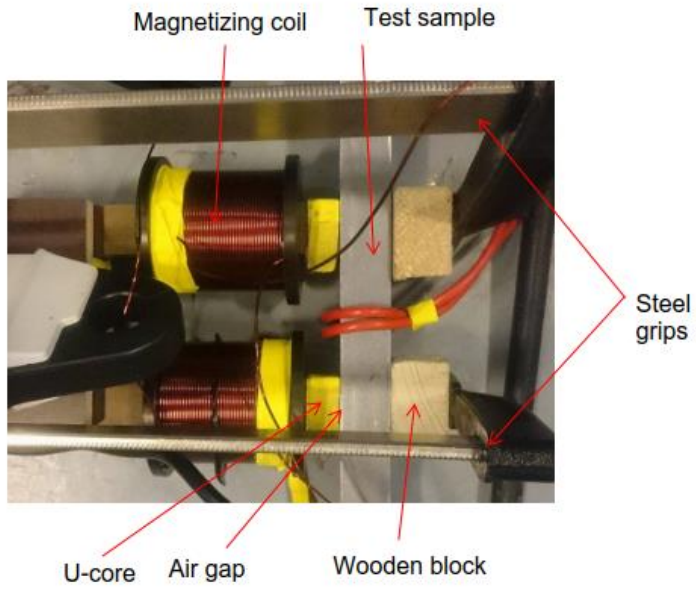

Figure 7.3: *Steel grips holding the test sample and the magnetizing coil.*

While applying cyclic loading, hydraulic press machine was utilized as discussed in Chapter 4. The hydraulic machine was capable of delivering static stress up till ±200 kN as it was designed to perform fatigue tests. The machine was not capable of providing cyclic stress at higher frequencies because the mechanical frame holding the machine was quite large. Various experiments were tried first to determine the suitable value for frequency for the cyclic stress. It was observed that when the frequency of the cyclic loading increases from 12 Hz the mechanical frame starts to vibrate causing distortion in the stress wave of cyclic loading. The waveform of cyclic loading at 20 Hz is given in Figure 7.4. The distortion also occurs while using higher amplitude of forces. The mechanical vibration from zero to 8 kN compression at 11 Hz is given in Figure 7.5.

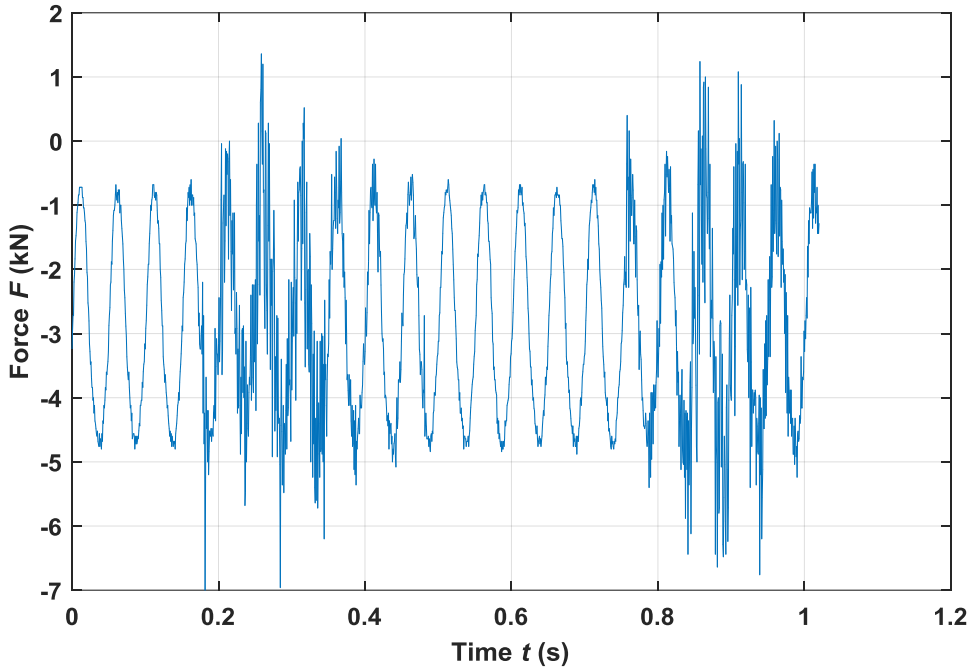

Figure 7.4: *Cycling loading at 20 Hz from -1kN to -5 kN.*

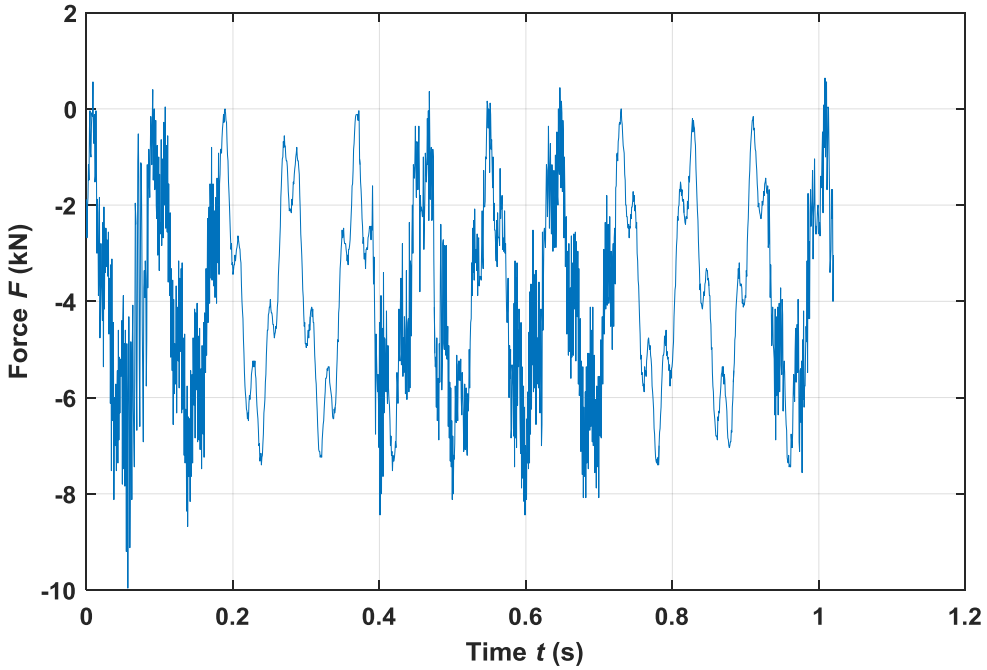

Figure 7.5: *Cyclic loading at 11 Hz from 0 kN to -8 kN.*

It was also observed that large amplitude of vibration (F > 10 kN) cannot be used while supplying cyclic loading at higher frequencies (f > 15 Hz). As evident from the above figures, the mechanical vibrations are not sinusoidal which affects the measured induced voltage under DC magnetization. The irregularity in mechanical vibration can be explained by various factors. The alignment of the mechanical grips, the backlash of the

hydraulic arm when the amplitude of the stress wave goes to zero and the resonant frequency of the vibrating frame causing distortion in the vibrations of hydraulic press machine. It was observed that mechanical grips holding the test sample have to be aligned so that the stress can only be applied parallel to the test sample. Because of the large size of the hydraulic press machine, it was not possible to accurately align the mechanical grips and a minor difference of 2 mm was observed in the alignment. Also, while performing dynamic stress tests at higher vibrational amplitudes (σ > 30 MPa), minor dis-alignment of mechanical grips occurred because of the slight buckling of the test sample. The dis-alignment was large for the test sample made up of steel sheets as compared to solid sample because of the maximum buckling load limit. It is known from the literature review from Chapter 2 that the induced voltage strongly depends upon the amplitude and frequency of the mechanical vibration. The induced voltage increases when the frequency of mechanical vibration increases, also the induced voltage increases when the stress amplitude is chosen such that it gives maximum ΔB as explained in Chapter 6. Due to the limitations of mechanical setup, the experiments were not carried out for higher frequencies and larger amplitudes of compressive and tensile stress.

The output voltage from the pickup coil was measured using digital oscilloscope under dynamic stress and DC magnetization as discussed in Chapter 4. It was observed that the output signal also contains noise signal of 50Hz (grid frequency noise) as well as high frequency noise signal on top of the base signal. The noise signal of 50 Hz was due to the grounding of the mechanical structure. The ground noise signal measured from the oscilloscope is given in figure 7.6.

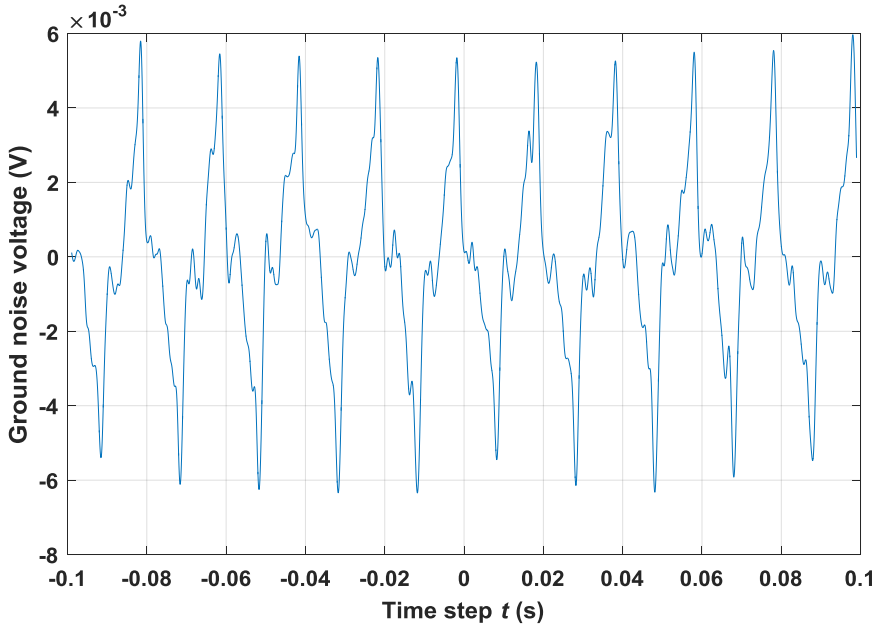

Figure 7.6: *Measured ground noise voltage.*

Thus, low pass filter was implemented using oscilloscope with the cutoff frequency of 80 Hz to digitally filter out the noise signal from the output signal. The measured output voltage from the pickup coil before and after filtration is given in Figure 7.7.

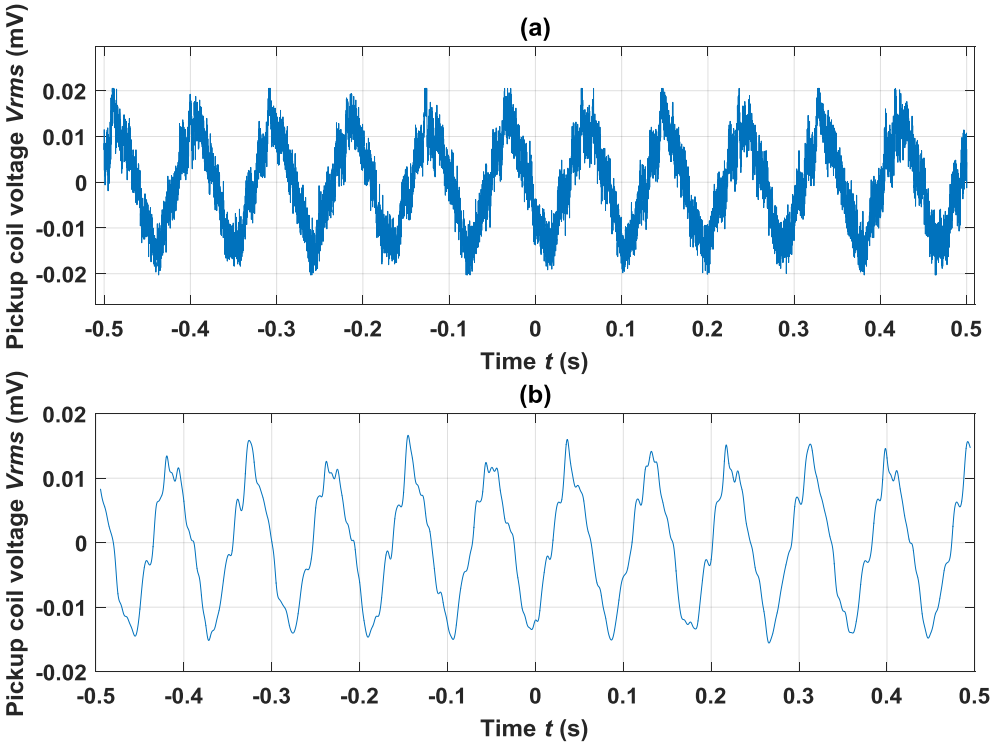

Figure 7.7: *Output voltage without filtration (a) and the output voltage after using low pass filter (b).*

The remaining noise present in the measured signal is due to the fact that the applied cyclic stress waveform was not pure sinusoidal as shown in Figure 7.5. Thus, the noise in the signal is the mechanical noise originated from hydraulic press machine.

While measuring pickup coil voltage under cyclic stress, it was observed that the test sample made up of steel sheets does not go into saturation because slight buckling causes the air gap between the plated to change, also, buckling causes the magnetic circuit length to chage continuously. The phenomenon was verified by testing the solid sample and repeating the same experiments. In case of solid bar, the induced voltage started decreasing when the material reaches saturation and the results are given in Chapter 6.

8. CONCLUSION

In this study, different energy harvesting techniques have been reviewed. Among all those techniques, the emphasis has been given to vibration based energy harvesting because of it growing popularity to develop self-powered systems. The concept of energy harvesting through magnetostrictive phenomena under ambient vibrations has been discussed in detail and a prototype energy harvester has been developed. The proposed energy harvester utilizes structural steel as an active material for harvesting energy. The idea was to harvest energy from construction material in buildings, bridges and rail tracks etc. having ferromagnetic properties and stress dependent magnetic characteristics. To do so, different test samples were constructed using a stack of steel sheets as well as a solid steel bar.

It was observed that the calculated buckling load can only be applied on solid sample during static stress test but for cyclic stress the maximum buckling load was reduced to one half. It was due to the fact that the hydraulic press machine was not capable of providing cyclic loading at higher stress values. The limitation of the hydraulic machine was the large supporting frame and size of the actuator. While obtaining *B*-*H* curves, the sample made up of steel sheets was utilized because the minimum frequency of the AC magnetization was 10 Hz and the amplifier could not provide sufficient current to magnetize the solid sample till saturation. The limitation for the minimum frequency was caused by the waveform control of the measurement method utilized during experimentation. Also, it was observed that the magnetizing current for solid bar at B = 1.35 T reached 6.71 A which exceeds the maximum current density of the magnetizing coil. From the static stress results it was concluded that the measured *B*-*H* curves for steel sheet sample can be utilized for solid steel bar as well provided the overall dimensions of the sample were the same.

During dynamic loading, the sample made of steel sheets was not going to saturation thus the dynamic tests were performed using solid steel bar. It was concluded that the induced voltage is directly proportional to the frequency of cyclic loading but due to the limitation of the experimental setup, high frequency mechanical vibrations were not possible. It was observed that the mechanical noise affects the induced voltage which could be seen as continuous fluctuation in the peak-to-peak value of the induced voltage. Also, it was observed that filtration of electrical noise from the signal reduces the amplitude of the measured voltage. The hysteresis curves plotted using DC magnetization under cyclic loading show residual flux when the applied magnetizing current was zero. Thus, it was concluded that the test sample should be demagnetized first before doing any new measurements in order to remove any residual flux to obtain accurate measurements. From the measured average power, it was concluded that structural steel can be utilized to harvest energy from low frequency mechanical vibrations. From experimental results it was concluded

that the applied compressive stress decreases the permeability of the material but due to design constraints the amplitude of applied stress was not enough to achieve maximum possible ΔB value. Thus, it was concluded that for higher compressive stress values, a supporting mechanism must be devised to prevent the sample from buckling.

The future work may focus on improving the mechanical design of the energy harvester. Determining the suitable construction material for energy harvesting having large magnetostrain. Determining the design parameters of a permanent magnet based on modeling and experimentation results. Designing the test sample in such way that same stress value can be achieved by applying small mechanical force reducing the size of the hydraulic machine and consequently reducing the noise in vibrations. The design of electronic circuitry for harvesting energy including switch mode converter design and the design of energy management system. The control system design for tracking the optimal value of mechanical vibration for efficient utilization of the energy harvester. Analyzing various vibration sources and development of possible modeling method. Testing under real world scenarios (prototyping) and improving the overall efficiency of energy harvesting device.

REFERENCES

[1] C. A. Howells, “Piezoelectric energy harvesting,” *Energy Convers. Manag.*, vol. 50, no. 7, pp. 1847–1850, 2009.

[2] P. D. Mitcheson, E. M. Yeatman, G. K. Rao, A. S. Holmes, and T. C. Green, “Energy harvesting from human and machine motion for wireless electronic devices,” *Proc. IEEE*, vol. 96, no. 9, pp. 1457–1486, 2008.

[3] F. Yildiz, “Potential Ambient Energy-Harvesting Sources and Techniques,” *J. Technol. Stud.*, pp. 40–48, 2007.

[4] A. Khaligh, S. Member, P. Zeng, S. Member, and C. Zheng, “Kinetic Energy Harvesting Using Piezoelectric and Electromagnetic Technologies — State of the Art,” vol. 57, no. 3, pp. 850–860, 2010.

[5] K. Matsubara, “Acceleration Technique of Waveform Control for Single Sheet Tester,” *IEEE Trans. Magn.*, vol. 31, no. 6, pp. 3400–3402, 1995.

[6] S. Boisseau, G. Despesse, and B. A. Seddik, “Electrostatic Conversion for Vibration Energy Harvesting,” *Small-Scale Energy Harvest.*, pp. 1–39, 2012.

[7] Y. Zhu and J. W. Zu, “Magnetoelectric Generator for Energy Harvesting From the Vibration of Magnetic Levitation,” vol. 48, no. 11, pp. 3344–3347, 2012.

[8] D. W. Harrist, “Wireless Battery Charging System Using Radio Frequency Energy Harvesting,” *Master’s thesis*, p. 60, University of Pittsburgh, 2004.

[9] M. Gueltig, M. Ohtsuka, H. Miki, T. Takagi, and M. Kohl, “Thermal energy harvesting by high frequency actuation of magnetic shape memory alloy films,” International Conference on Solid-State Sensors, Actuators and Microsystems pp. 718–721, 2015.

[10] R. E. Blankenship, D. M. Tiede, J. Barber, G. W. Brudvig, G. Fleming, M. Ghirardi, M. R. Gunner, W. Junge, D. M. Kramer, A. Melis, T. a Moore, C. C. Moser, D. G. Nocera, A. J. Nozik, D. R. Ort, W. W. Parson, R. C. Prince, and R. T. Sayre, “Comparing photosynthetic and photovoltaic efficiencies and recognizing the potential for improvement.,” *Science*, vol. 332, no. 6031, pp. 805–9, 2011.

[11] M. J. Dapino, “On Magnetostrictive Materials and Their Use in Smart Material Transducer,” *Struct. Eng. Mech. J.*, pp. 1–28, 2002.

[12] A. Ledoux, “Theory of Piezoelectric Materials and Their Applications in Civil Engineering,” p. 49, 2011.

[13] G. Engdahl, “Magnetostrictive Material and Actuator Characterization,” pp. 0–12.

[14] B. Bhattacharya, “Terfenol and Galfenols : Smart Magnetostrictive Metals for Intelligent Transduction,” *Dir. Mag. (Indian Inst. od Technol. Kanpur)*, vol. 7, no. 2, pp. 35–40, 2005.

[15] A. G. Olabi and A. Grunwald, “Design and Application of Magnetostrictive ‘ MS ’ Materials,” vol. i, pp. 1–30.

[16] A. Bayrashev, A. Parker, W. P. Robbins, and B. Ziaie, “Low frequency wireless powering of microsystems using piezoelectric-magnetostrictive laminate composites,” *Transducers., 12th Int. Conf. Solid-State Sensors, Actuators Microsystems, Dig. Tech. Pap.*, vol. 2, pp. 1707–1710, 2003.

[17] D. Davino. A. Giustinian, C. Visone, “Stress-Induced Eddy Currents in Magnetostrictive Energy Harvesting Devices,” *IEEE Trans. Magn.*, vol. 48, no. 1, pp. 18–25, 2012.

[18] “Smart materials Piezoelectric materials Shape memory materials “ smart technology. Presentation, slide 9.

[19] R. B. Williams, G. Park, D. J. Inman, and W. K. Wilkie, “An Overview of Composite Actuators with Piezoceramic Fibers,” *2002 IMAC-XX Conf. Expo. Struct. Dyn.*, pp. 421–427, 2002.

[20] S. Roundy, P. K. Wright, and K. S. J. Pister, “Micro-electric vibration-to-electricity converters,” *Proc. ASME Int. Mech. Eng. Congr. Expo.*, pp. 1–10, 2002.

[21] S. Roundy and P. K. Wright, “A piezoelectric vibration based generator for wireless electronics,” *Smart Mater. Struct.*, vol. 13, no. 5, pp. 1131–1142, 2004.

[22] C. B. Williams and R. B. Yates, “Analysis Of A Micro-electric Generator For Microsystems,” *Proc. Int. Solid-State Sensors Actuators Conf. - Transducers.*, vol. 1, pp. 8–11, 1995.

[23] R. Amirtharajah and A. P. Chandrakasan, “Self-powered signal processing using vibration-based power generation,” *IEEE J. Solid-State Circuits*, vol. 33, no. 5, pp. 687–695, 1998.

[24] F. Claeyssen, “Magnetostrictive actuators compared to piezoelectric actuators,” *Proc. SPIE Eur. Work. Smart Struct. Eng. Technol.*, pp. 194–200, 2003.

[25] N. S. Shenck and J. a Paradiso, “Energy Scavenging With Shoe-Mounted Piezoelectrics Electricity From the Forces Exerted on a Shoe During Walking,” *IEEE Micro*, pp. 30–42, 2001.

[26] T. Starner, “Human-powered wearable computing,” *IBM Syst. J.*, vol. 35, no. 3.4, pp. 618–629, 1996.

[27] D. G. Larsen, “Structural Health Monitoring Of Composite Structures Using Magnetostrictive Sensors And Actuators,” Doctoral Thesis, Indian Institute of Science Bangalore October, 2016.

[28] G. Despesse, J. J. Chaillout, T. Jager, J. M. Léger, a. Vassilev, S. Basrour, “High

damping electrostatic system for vibration energy scavenging," *Proc. 2005 Jt. Conf. Smart objects Ambient Intell. Innov. Context. Serv. usages Technol.*, pp. 283-286. ACM, 2005.

[29] H. Li, C. Tian, and Z. D. Deng, "Energy harvesting from low frequency applications using piezoelectric materials," *Appl. Phys. Rev.*, vol. 1, no. 4, pp. 0–20, 2014.

[30] S. Roundy, P. K. Wright, and J. Rabaey, "A study of low level vibrations as a power source for wireless sensor nodes," *Comput. Commun.*, vol. 26, no. 11, pp. 1131–1144, 2003.

[31] D. Kwon, J. Park, and K. Law, "Electromagnetic energy harvester with repulsively stacked multilayer magnets for low frequency vibrations," *Smart Mater. Struct*, vol. 22, pp. 55007–12, 2013.

[32] J. Gauthier, A. Hubert, N. Chaillet, "Magnetic Shape Memory Alloy and Actuator Design," , Intern Workshop on Microfactories, *IWMF 06*. October 2008.

[33] M. Kohl, D. Brugger, M. Ohtsuka, and T. Takagi, "A novel actuation mechanism based on ferromagnetic SMA thin films," *Transducers. - 12th Int. Conf. Solid-State Sensors, Actuators Microsystems, Dig. Tech. Pap.*, vol. 2, pp. 1011–1014, 2003.

[34] S. Dong, J. Zhai, J. F. Li, D. Viehland, and S. Priya, "High power density magnetoelectric energy harvester," in *2008 17th IEEE International Symposium on the Applications of Ferroelectrics*, 2008, vol. 1, pp. 1–2.

[35] N. S. Shenck, "A Demonstration of Useful Electric Energy Generation from Piezoceramics in a Shoe by," Diss. Massachusetts Institute of Technology, pp. 1–137, 1999.

[36] M. Renaud, T. Sterken, "Scavenging Energy From Human Body Design of a Piezoelectric Transducer," *Digest of Technical Papers. IEEE Transducers.,* Vol. 1. pp. 784–787, 2005.

[37] Z. Zhang, H. Xiang, and Z. Shi, "Modeling on piezoelectric energy harvesting from pavements under traffic loads," *J. Intell. Mater. Syst. Struct.*, vol. 27, no. 4, pp. 567–578, 2015.

[38] V. Berbyuk and J. Sodhani, "Towards modelling and design of magnetostrictive electric generators," *Comput. Struct.*, vol. 86, no. 3–5, pp. 307–313, 2008.

[39] J. L. Wardlaw, I. Karaman, and A. I. Karsilayan, "Low-power circuits and energy harvesting for structural health monitoring of bridges," *IEEE Sensors Journal*, vol. 13, no. 2, pp. 709–722, 2013.

[40] M. Zucca, A. Hadadian, and O. Bottauscio, "Quantities affecting the behavior of vibrational magnetostrictive transducers," *IEEE Trans. Magn.*, vol. 51, no. 1, pp. 2–5, 2015.

[41] O. Bottauscio, A. Lovisolo, P. E. Roccato, M. Zucca, C. Sasso, R. Bonin, "Modeling and Experimental Analysis of Magnetostrictive Devices : From the

Material Characterization to Their Dynamic Behavior," *IEEE Trans. Magn.*, vol. 44, no. 11, pp. 3009–3012, 2008.

[42] I. Clausen and T. Glott, "Development of clinically relevant implantable pressure sensors: perspectives and challenges.," *Sensors*, vol. 14, no. 9, pp. 17686–702, 2014.

[43] STMicroelectronics, "STLM20 - Ultra-low current 2.4 V precision analog temperature sensor," *Data Sheet*, no. July, pp. 1–19, 2010.

[44] G. T. Hwang, H. Park, J. H. Lee, S. Oh, K. Il Park, M. Byun, H. Park, G. Ahn, C. K. Jeong, K. No, H. Kwon, S. G. Lee, B. Joung, and K. J. Lee, "Self-powered cardiac pacemaker enabled by flexible single crystalline PMN-PT piezoelectric energy harvester," *Adv. Mater.*, vol. 26, no. 28, pp. 4880–4887, 2014.

[45] P. D. Bradley, "An Ultra Low Power, High Performance Medical Implant Communication System (MICS) Transceiver for Implantable Devices," *IEEE Biomed. Circuits Syst. Conf. BioCAS*, pp. 158–161, 2006.

[46] S. Xu, Y. W. Yeh, G. Poirier, M. C. McAlpine, R. A. Register, and N. Yao, "Flexible piezoelectric PMN-PT nanowire-based nanocomposite and device," *Nano Lett.*, vol. 13, no. 6, pp. 2393–2398, 2013.

[47] H. A. Sodano, "Development of an Automated Eddy Current Structural Health Monitoring Technique with an Extended Sensing Region for Corrosion Detection," *Struct. Heal. Monit.*, vol. 6, no. 2, pp. 111–119, 2007.

[48] Y. B. Yang and C. W. Lin, "Vehicle-bridge interaction dynamics and potential applications," *J. Sound Vib.*, vol. 284, no. 1–2, pp. 205–226, 2005.

[49] J. C. Chin, J. M. Rautenberg, C. Y. T. Ma, S. Pujol, and D. K. Y. Yau, "An experimental low-cost, low-data-rate rapid structural assessment network," *IEEE Sens. J.*, vol. 9, no. 11, pp. 1361–1369, 2009.

[50] J. L. Wardlaw, I. Karaman, and A. I. Karşilayan, "Low-power circuits and energy harvesting for structural health monitoring of bridges," *IEEE Sens. J.*, vol. 13, no. 2, pp. 709–722, 2013.

[51] H. Janocha, "Application potential of magnetic field driven new actuators," *Sensors Actuators, A Phys.*, vol. 91, no. 1–2, pp. 126–132, 2001.

[52] R. Dhilsha, P. M. Rajeshwari, and V. Rajendran, "Advanced magnetostrictive materials for sonar applications," *Def. Sci. J.*, vol. 55, no. 1, pp. 13–20, 2005.

[53] Z. Deng, V. M. Asnani, and M. J. Dapino, "Magnetostrictive vibration damper and energy harvester for rotating machinery," *SPIE Smart Structures and Materials+ Nondestructive Evaluation and Health Monitoring*, vol. 9433, p. 94330C, 2015.

[54] D. A. Bushko and J. H. Goldie, "High Performance Magnetostrictive Actuators," *IEEE Aerosp. Electron. Syst. Mag.*, vol. 6, no. 11, pp. 21–25, 1991.

[55] Z Kaczkowski, É. Kisdi-Koszó, and L. Potocký. "Magnetomechanical coupling in

the Fe85B15 amorphous alloy ribbons produced in longitudinal and transverse field during quenching." *Le Journal de Physique Colloques* 49. C8-1351. 1988.

[56] M. Avcar, "Elastic Buckling of Steel Columns Under Axial Compression," *Am. J. Civ. Eng.*, vol. 2, no. 3, p. 102, 2014.

[57] H. Mohamed and H. Aziz, "An Appraisal of Euler and Johnson Buckling theories under dynamic compression buckling loading," *Iraqi J. Mech. Mater*, vol. 9, no. 2, pp. 173–181, 2007.

[58] A. N. Al-khazraji, S. A. Al-rabii, and H. S. Al-khazalli, "Enhancement of Buckling Resistance of Aluminized Long Columns of Stainless Steel", AISI 303," vol. 12, no. 1, 2016.

[59] R. L. Boylestad, "Introductory circuit analysis," vol 11, pp. 513-528, 2003.

[60] S. Zurek, P. Marketos, T. Meydan, and A. J. Moses, "Magnetic Measurements Under Controlled Magnetizing Conditions," vol. 41, no. 11, pp. 4242–4249, 2005.

[61] S. Zurek, Stan, and T. Meydan. "Digital feedback controlled RSST system." *Proc. 16th SMM Conf*. 2004.

[62] T. Yamasaki, S. Yamamoto, and M. Hirao, "Effect of applied stresses on magnetostriction of low carbon steel," *NDT E Int.*, vol. 29, no. 5, pp. 263–268, 1996.